JGR Solid Earth

RESEARCH ARTICLE

10.1029/2025JB031240

Transient Propagation of Ductile Ruptures by Thermal Runaway

A. Spang[1], **M. Thielmann**[1,2], **A. de Montserrat**[3], and **T. Duretz**[4]

[1]Bayerisches Geoinstitut, Universität Bayreuth, Bayreuth, Germany, [2]Institut für Geowissenschaften, Universität Bonn, Bonn, Germany, [3]Department of Earth Sciences, ETH Zürich, Zürich, Switzerland, [4]Faculty of Earth Sciences, Goethe University, Frankfurt am Main, Germany

Key Points:

- 2D thermomechanical, visco-elastic models resolve nucleation and propagation of transient ductile ruptures driven by thermal runaway
- Ductile ruptures can reach seismic velocities for mantle transition zone conditions, in line with deep-focus earthquake locations
- Ductile creep events near the brittle-ductile transition can cause pressure perturbations sufficient to induce brittle earthquakes

Supporting Information:

Supporting Information may be found in the online version of this article.

Correspondence to:

A. Spang,
arne.spang@uni-bayreuth.de

Citation:

Spang, A., Thielmann, M., de Montserrat, A., & Duretz, T. (2025). Transient propagation of ductile ruptures by thermal runaway. *Journal of Geophysical Research: Solid Earth*, *130*, e2025JB031240. https://doi.org/10.1029/2025JB031240

Received 31 JAN 2025
Accepted 16 JUN 2025

Author Contributions:

Conceptualization: A. Spang, M. Thielmann, T. Duretz
Data curation: A. Spang
Formal analysis: A. Spang
Funding acquisition: M. Thielmann
Investigation: A. Spang
Methodology: A. Spang, M. Thielmann
Project administration: M. Thielmann
Resources: M. Thielmann
Software: A. Spang, A. de Montserrat
Validation: A. Spang
Visualization: A. Spang
Writing – original draft: A. Spang
Writing – review & editing: A. Spang, M. Thielmann, A. de Montserrat, T. Duretz

Abstract Ductile deformation is typically associated with slow and steady-state deformation, yet the occurrence of deep earthquakes, which exhibit a rapid and transient behavior, challenges this view. One proposed mechanism to facilitate such behavior is thermal runaway. However, two-dimensional (2D) models that capture highly localized, transient ductile deformation, driven by thermal runaway, remain unexplored. This study presents 2D simple shear models using the pseudo-transient relaxation method optimized for graphics processing units. The models incorporate a Maxwell rheology including compressible elasticity, diffusion creep, dislocation creep, and low-temperature plasticity. Our models capture the nucleation and transient propagation of highly localized ductile ruptures driven by thermal runaway. Depending on rheological parameters, we observe a spectrum of behaviors: (a) broad shear zones which deform only slightly faster than the boundary conditions; (b) localized deformation which is orders of magnitude faster than far field deformation; and (c) highly localized ruptures reaching seismic slip velocities. Runaway intensity scales with nondimensional numbers derived from 1D studies, but its spatial and temporal evolution is more complex, traversing several stages. The rupture front perturbs the local stress field, generating opposing pressure anomalies of up to 1.5 GPa. For mantle transition zone conditions, thermal runaway-driven ductile ruptures can reach seismic slip velocities, confirming it as a viable mechanism for deep-focus earthquakes. Under brittle-ductile transition zone conditions, our models capture thermal runaway driving accelerated creep which disturbs the local pressure field sufficiently to facilitate brittle failure in an otherwise ductile host rock.

Plain Language Summary Ductile deformation is usually slow and consistent, but earthquakes in hundreds of km depth suggest that it can also be fast and irregular. Thermal runaway is a mechanism that could help explain this behavior, but no previous models have been able to demonstrate this. Our simulations consider various ways rocks deform, including elasticity and different creep mechanisms. We found that thermal runaway can create slow, broad zones of deformation, more localized accelerated creep, or very fast, earthquake-like ruptures. The overall behavior of our models is controlled by the same parameters as 1D models, but our results show that the evolution is much more complex in 2D, progressing through different stages. The rupture fronts also create significant changes in pressure and stress nearby, with pressure anomalies reaching up to 1.5 GPa. In the mantle, thermal runaway can produce fast ruptures, similar to deep-focus earthquakes. Near the brittle-ductile transition zone, thermal runaway may drive creep events that destabilize surrounding rocks enough to trigger brittle failure. Our findings provide new insights into how rapid, viscous deformation by thermal runaway can contribute to deep-focus earthquakes in the mantle transition zone and small earthquakes at the brittle-ductile transition zone.

1. Introduction

Ductile deformation describes a variety of different ways for material to accommodate strain, and its exact definition varies among different fields of research (Fossen & Cavalcante, 2017; Paterson & Wong, 2005; Twiss & Moores, 2007). Usually, it is associated with slow and uniform processes like mantle convection, and Rutter (1986) defines ductility as non-localized flow. Other studies point out that localization can occur due to ductile instabilities (e.g., Hobbs et al., 1986; Misra & Mandal, 2007; Poirier, 1980), resulting in non-uniform and significantly faster deformation. Karato (2008) even proposes the term “ductile faulting.” Here, we use the term “ductile” to describe irreversible (i.e., non-elastic) and fracture-free (i.e., non-brittle) deformation with a defined relationship between stress and strain rate (Paterson & Wong, 2005; Twiss & Moores, 2007).

As ductile deformation is sensitive to temperature and strain rate (e.g., Hirth & Kohlstedt, 2003), it is prone to instability and localization (Gruntfest, 1963; Hobbs et al., 1990; Poirier, 1980). This means that deformation is not uniformly distributed in a body, but concentrates into a thin zone which separates two relatively stiff blocks. Such shear bands or shear zones exist in many different materials such as metals (e.g., Antolovich & Armstrong, 2014), polymers (e.g., L. Zhang et al., 2021), and geomaterials (e.g., Desrues et al., 2007). Localization occurs on all scales from mineral grains (10^{-6} m) to tectonic plate boundaries (10^{6} m) (Fossen & Cavalcante, 2017; Hobbs et al., 1990; Poirier, 1980; Tchalenko, 1970).

One example for ductile localization are mylonites. Estimates for the deformation rate of mylonites are as high as 10^{-9} m s^{-1} (Hacker et al., 1990; Okudaira & Shigematsu, 2012), which is line with the velocity of tectonic plates. Slow slip events (SSEs), sometimes referred to as creep events, slow or silent earthquakes, cover the range between tectonic plates and earthquakes (10^{-4}–1 m s^{-1}, Bürgmann, 2018; Kirkpatrick et al., 2021; Weng & Ampuero, 2022). While these events are predominantly attributed to frictional sliding in the brittle regime (Bürgmann, 2018; Schwartz & Rokosky, 2007; Segall et al., 2010), some instances are also associated with ductile deformation (Behr et al., 2018; Bürgmann, 2018; Fagereng et al., 2014; Hayman & Lavier, 2014; Reber et al., 2015). Going forward, we will refer to this velocity range as accelerated creep (AC). Finally, the existence of intermediate-depth (70–300 km) and deep-focus (300–700 km) earthquakes implies that ductile deformation may even drive deformation in the velocity range of seismic events $\left(10^{-4}-1 \text{ m s}^{-1}\right)$. These events are difficult to reconcile with our understanding of brittle failure (e.g., Byerlee, 1978; Drucker & Prager, 1952) which suggests that they are driven by rapid ductile localization. So, not only does ductile deformation cover spatial scales of μm to km, it may also operate on time scales of seconds to millions of years.

Especially for the rapid deformation during deep earthquakes, a specific localization mechanism is necessary. Experimental studies have established dehydration embrittlement (e.g., Hacker et al., 2003; Meade & Jeanloz, 1991; Raleigh & Paterson, 1965) and transformational faulting (Burnley et al., 1991; Gasc et al., 2022; Green & Burnley, 1989; Kirby, 1987; Kirby et al., 1996; Rubie & Ross, 1994; Schubnel et al., 2013; Wang et al., 2017) as viable mechanisms for intermediate-depth and deep-focus earthquakes respectively. Thermal runaway is the third mechanism which is commonly associated with all earthquakes outside the brittle domain (Frohlich, 1989; Houston, 2015; Zhan, 2020). It is based on the positive feedback loop between deformation, viscous dissipation, temperature-dependent viscosity, and localization (Gruntfest, 1963). Reproducing it in high-pressure experiments is challenging because of the size of experimental samples and the controlled temperature conditions. Therefore, numerical models are necessary to assess its viability.

Several two- and three-dimensional (2D and 3D) numerical studies have shown that thermal runaway or thermal weakening can result in lithosphere-scale shear zones (Jaquet et al., 2016; Kaus & Podladchikov, 2006; Kiss et al., 2019; Regenauer-Lieb & Yuen, 2004; Schmalholz & Duretz, 2015; Thielmann & Kaus, 2012). However, these large-scale studies lack the spatial and temporal resolution to capture the propagation of ductile ruptures. Furthermore, they employ minimum viscosities on the order of 10^{18} Pa s (Piccolo et al., 2019; Thielmann & Kaus, 2012) which inhibits the necessary level of localization for deformation rates beyond the scale of plate tectonics (Spang et al., 2024).

A large number of one-dimensional (1D) studies have demonstrated that thermal runaway can lead to rapid stress release and large slip velocities (e.g., Braeck et al., 2009; Braun et al., 1999; John et al., 2009; Kelemen & Hirth, 2007; Ogawa, 1987; Spang et al., 2024; Thielmann, 2018; Thielmann et al., 2015; Yuen et al., 1978). However, the geometry of these models implies that a thermally weakened zone extends infinitely in the other spatial dimensions, so they cannot account for its propagation. In reality, a rupture front has to propagate through intact rock by weakening it, and 1D models may underestimate the time and energy this requires. 2D and 3D studies which focus on thermal runaway (e.g., Duretz et al., 2015, 2019; Kaus & Podladchikov, 2006; Kiss et al., 2019) show the development of a steady state shear zone but are not able to capture a highly localized rupture front.

This questions the viability of thermal runaway-driven deep earthquakes (70–700 km depth). Here, we investigate whether highly localized shear zones can nucleate at small perturbations and propagate due to thermal runaway in 2D. Our models aim to capture the transient propagation of ductile ruptures and quantify the slip velocities they achieve as well as the stress field they impose on their host rock. We investigate two applications, the brittle-ductile transition zone and the mantle transition zone. As part of that, we explore the parameter space given by the uncertainty of the pressure dependence of low-temperature plasticity (LTP) and the grain size of cold slab cores.

2. Methods

2.1. Governing Equations

Our model is an extension of the work of Spang et al. (2024) and is governed by the following system of coupled equations:

$$\frac{\partial \tau_{ij}}{\partial x_j} - \frac{\partial P}{\partial x_i} = 0, \tag{1}$$

$$\frac{1}{\rho}\frac{d\rho}{dt} = -\frac{\partial v_i}{\partial x_i}, \tag{2}$$

$$\rho C_p \frac{dT}{dt} = \lambda \frac{\partial^2 T}{\partial {x_i}^2} + \tau_{ij}\dot{\varepsilon}_{ij}^{\mathrm{vi}}, \tag{3}$$

$$\frac{1}{K_{\mathrm{b}}}\frac{dP}{dt} = -\frac{\partial v_i}{\partial x_i}, \tag{4}$$

$$\dot{\varepsilon}_{ij} = \frac{1}{2}\left(\frac{\partial v_i}{\partial x_j} + \frac{\partial v_j}{\partial x_i}\right) - \frac{1}{3}\frac{\partial v_k}{\partial x_k}\delta_{ij}, \tag{5}$$

$$\dot{\varepsilon}_{ij} = \dot{\varepsilon}_{ij}^{\mathrm{el}} + \dot{\varepsilon}_{ij}^{\mathrm{vi}} = \frac{1}{2G}\frac{d\tau_{ij}}{dt} + \frac{1}{2\eta}\tau_{ij}, \tag{6}$$

where τ_{ij} is the Cauchy stress deviator, $x_i(i = 1,2)$ denotes the Cartesian coordinates, P is pressure (positive in compression), ρ density, t time, v_i the velocity vector, C_p specific heat capacity, T temperature, λ thermal conductivity, $\dot{\varepsilon}_{ij}$ the deviatoric strain rate, $\dot{\varepsilon}_{ij}^{\mathrm{el}}$ and $\dot{\varepsilon}_{ij}^{\mathrm{vi}}$ its elastic and viscous components respectively, K_{b} bulk modulus, δ_{ij} the Kronecker-Delta, G shear modulus, and η effective nonlinear viscosity (see Section 2.2.2).

Equations 1–3 describe the conservation of momentum, mass, and energy, respectively. For simplicity, we neglect inertial terms, body forces (i.e., gravity), thermal expansion, as well as adiabatic and radiogenic heating. The last term of Equation 3 represents shear heating (i.e., heat release from viscous dissipation). Equations 4–6 are constitutive relationships concerning compressibility (Equation 4), deformation (Equation 5), and Maxwell visco-elasticity (Equation 6). We investigated the influence of thermal expansion and adiabatic heating, and found their contribution to be minor (see Text S1.1 and Figure S1 in Supporting Information S1).

2.2. Implementation

We discretize Equations 1–6 on a staggered grid using the small-strain approximation and finite differences (Figure 1a, e.g., Gerya & Yuen, 2003). The equations are solved with the damped pseudo-transient approach (e.g., Duretz et al., 2019; Frankel, 1950; Räss et al., 2022). The code is written in the Julia programming language and utilizes the package GeoParams.jl (Kaus et al., 2023) to non-dimensionalize physical parameters and ParallelStencil.jl (Omlin & Räss, 2024) for GPU-parallelization. To resolve the self-feeding runaway process, we use an adaptive time stepping scheme. If local temperature changes exceed 50 K within one time step, the time step is reduced and the solver restarted.

2.2.1. Pseudo-Transient Approach

In the pseudo-transient approach, the conservation equations are solved at every physical time step by introducing a pseudo-time derivative for each equation and iteratively incrementing the primary variables v, P, and T until the residuals are smaller than a given numerical tolerance. Applying this procedure to Equations 1–3 yields

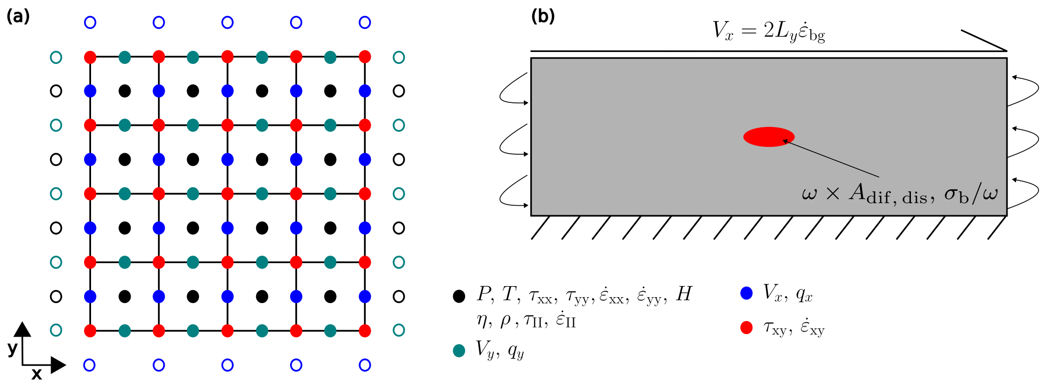

Figure 1. Numerical grid and geometrical setup. (a) Illustration of the staggered numerical grid, where colored dots show where physical properties are defined. Hollow circles are ghost nodes outside the physical domain that are necessary to apply boundary conditions. (b) Model setup. Left and right boundaries are periodic. Bottom boundary is no slip and top boundary enforces simple shear. Not to scale.

$$\frac{\partial v_i}{\partial \psi} = \frac{\partial \tau_{ij}}{\partial x_j} - \frac{\partial P}{\partial x_i}, \tag{7}$$

$$\frac{\partial P}{\partial \psi} = \frac{1}{K_{\mathrm{b}}}\frac{dP}{dt} + \frac{\partial v_i}{\partial x_i} \tag{8}$$

$$\frac{\partial T}{\partial \psi} = \frac{\lambda \frac{\partial^2 T}{\partial x_i^2} + \tau_{ij}\dot{\varepsilon}_{ij}^{\mathrm{vi}}}{\rho C_p} - \frac{dT}{dt}, \tag{9}$$

where $\frac{\partial}{\partial \psi}$ denotes the pseudo-time derivative of a parameter. During each pseudo-time iteration, each primary variable is incremented proportionally to the sum of the current residual and the previous increment (Duretz et al., 2019).

$$\Delta_\gamma = \left[\frac{\partial \gamma}{\partial \psi} + \left(1 - \frac{1}{\zeta_\gamma}\right)\Delta_\gamma^{\mathrm{prev}}\right]\Delta\psi_\gamma, \tag{10}$$

where γ is either v_x, v_y, P or T. Δ_γ is the increment to the respective variable, $\Delta_\gamma^{\mathrm{prev}}$ is the increment of the previous iteration, ζ_γ is the damping parameter (>1), and $\Delta\psi_\gamma$ is the size of the pseudo-time step.

2.2.2. Rheology

Viscous deformation is assumed to be a combination of diffusion creep, dislocation creep, and LTP:

$$\dot{\varepsilon}_{\mathrm{II}}^{\mathrm{vi}} = \dot{\varepsilon}_{\mathrm{II}}^{\mathrm{dif}} + \dot{\varepsilon}_{\mathrm{II}}^{\mathrm{dis}} + \dot{\varepsilon}_{\mathrm{II}}^{\mathrm{LTP}}, \tag{11}$$

where the superscripts $^{\mathrm{dif}}$, $^{\mathrm{dis}}$, and $^{\mathrm{LTP}}$ denote diffusion creep, dislocation creep, and LTP, respectively, and the subscript $_{\mathrm{II}}$ denotes the square root of the second invariant of the respective tensor.

$$\dot{\varepsilon}_{\mathrm{II}}^{\mathrm{vi}} = \sqrt{\frac{1}{2}\dot{\varepsilon}_{ij}^{\mathrm{vi}}\ \dot{\varepsilon}_{ij}^{\mathrm{vi}}} \tag{12}$$

Consequently, the effective viscosity η can be expressed as

$$\eta = \left(\frac{1}{\eta_{\mathrm{dif}}} + \frac{1}{\eta_{\mathrm{dis}}} + \frac{1}{\eta_{\mathrm{LTP}}}\right)^{-1}, \tag{13}$$

$$\eta_{\mathrm{dif}} = \frac{1}{2}(A_{\mathrm{dif}})^{-1} d^{m} e^{\frac{E_{\mathrm{dif}}+PV_{\mathrm{dif}}}{RT}} \frac{F_1}{F_2}, \tag{14}$$

$$\eta_{\mathrm{dis}} = \frac{1}{2}(A_{\mathrm{dis}})^{-\frac{1}{n}} \left(\dot{\varepsilon}_{\mathrm{II}}^{\mathrm{dis}}\right)^{\frac{1}{n}-1} e^{\frac{E_{\mathrm{dis}}+PV_{\mathrm{dis}}}{nRT}} \frac{F_1^{\frac{1}{n}}}{F_2}, \tag{15}$$

$$\eta_{\mathrm{LTP}} = \frac{\tau_{\mathrm{LTP}}}{2\,\dot{\varepsilon}_{\mathrm{II}}^{\mathrm{LTP}}}, \tag{16}$$

where A are pre-factors, E are activation energies, and V are activation volumes of the respective flow laws. d is the grain size, m the grain size exponent of diffusion creep, R the universal gas constant, and n the powerlaw exponent of dislocation creep. $F_1 = \frac{2}{\sqrt{3}}$ and $F_2 = \sqrt{3}$ are factors for the conversion from axial strain rate and stress in experiments to deviatoric strain rate and stress (Gerya, 2019). The LTP–stress τ_{LTP} is given by

$$\tau_{\mathrm{LTP}} = \frac{RT}{E_{\mathrm{LTP}} + PV_{\mathrm{LTP}}} \frac{\sigma_{\mathrm{res}}}{F_2} \sinh^{-1}\left(\frac{\dot{\varepsilon}_{\mathrm{II}}^{\mathrm{LTP}} F_1}{A_{\mathrm{LTP}}} e^{\frac{E_{\mathrm{LTP}}+PV_{\mathrm{LTP}}}{RT}}\right) + \frac{\sigma_{\mathrm{b}}}{F_2}, \tag{17}$$

$$\sigma_{\mathrm{res}} = \sigma_{\mathrm{L}} + \frac{\sigma_{\mathrm{K}}}{\sqrt{d}}, \tag{18}$$

where σ_{b}, σ_{L}, and σ_{K} are material constants (Hansen et al., 2019). This is only one of several flow laws for LTP (Jain et al., 2017; Kumamoto et al., 2017; Toffol et al., 2022). We discuss our choice in Text S2 in Supporting Information S1.

Given the nonlinear nature of dislocation creep and LTP, the strain rate partitioning (Equation 11) cannot be solved analytically but requires an iterative approach. It can be updated and solved alongside the conservation Equations 7–9. Once the left hand side terms in Equations 7–9, as well as the residual of Equation 11 are smaller than the tolerance, the solution is converged.

To stabilize the model during thermal runaway and limit mesh-dependencies, we use the regularization approach of Spang et al. (2024) which adds a term to Equation 13:

$$\eta = \left(\frac{1}{\eta_{\mathrm{dif}}} + \frac{1}{\eta_{\mathrm{dis}}} + \frac{1}{\eta_{\mathrm{LTP}}}\right)^{-1} + \eta_{\mathrm{reg}}, \tag{19}$$

where η_{reg} is the regularization viscosity, a numerical parameter which provides a lower limit for the viscosity. We use $\eta_{\mathrm{reg}} = 10^{12}$ Pa s which is low enough to not inhibit thermal runaway (Spang et al., 2024).

The density in the model is a function of the pressure P and the Poisson's ratio ν:

$$\rho = \rho_0\, e^{\frac{P}{K_{\mathrm{b}}}}, \tag{20}$$

$$K_{\mathrm{b}} = \frac{2G(1+\nu)}{3(1-2\nu)}, \tag{21}$$

where K_{b} is the bulk modulus.

2.3. Model Setup

In Figure 1b, we show our model setup with horizontal extent $L_{\mathrm{x}} = 60$ km and vertical extent $L_{\mathrm{y}} = 10$ km. We enforce a no slip boundary condition ($v_x = v_y = 0$) at the bottom, a kinematic boundary condition $\left(v_x = 2L_{\mathrm{y}}\dot{\varepsilon}_{\mathrm{bg}},\ v_y = 0\right)$ at the top of the domain, and periodic boundary conditions at the lateral boundaries. These boundary conditions allow us to also investigate cases with two anomalies as ruptures propagating away from the

Table 1
Material Parameters for Reference Model

Parameter	Unit	Value
T_0	$[°C]$	650
P_0	[GPa]	20
$\dot{\varepsilon}_{\mathrm{bg}}$	$[\mathrm{s}^{-1}]$	2×10^{-13}
ρ_0	$[\mathrm{kg\ m}^{-3}]$	3,300
d	[µm]	1[j]
η_{reg}	[Pa s]	10^{12}
G	[GPa]	100[a,b]
m		3[c]
A_{dif}	$[\mu\mathrm{m}^{m}\ \mathrm{MPa}^{-1}\ \mathrm{s}^{-1}]$	1.5×10^{9}[c]
E_{dif}	$[\mathrm{kJ\ mol}^{-1}]$	375[c]
V_{dif}	$[\mathrm{cm}^3\ \mathrm{mol}^{-1}]$	6[c]
n		3.5[c]
A_{dis}	$[\mathrm{MPa}^{-n}\ \mathrm{s}^{-1}]$	1.1×10^{5}[c]
E_{dis}	$[\mathrm{kJ\ mol}^{-1}]$	530[c]
V_{dis}	$[\mathrm{cm}^3\ \mathrm{mol}^{-1}]$	15[c,d]
A_{LTP}	$[\mathrm{s}^{-1}]$	5×10^{20}[e]
E_{LTP}	$[\mathrm{kJ\ mol}^{-1}]$	530[f]
V_{LTP}	$[\mathrm{cm}^3\ \mathrm{mol}^{-1}]$	15[f]
σ_{L}	[GPa]	3.1[e]
σ_{K}	$[\mathrm{GPa}\ \mu\mathrm{m}^{0.5}]$	3.2[e]
σ_{b}	[GPa]	1.8[e]
C_p	$[\mathrm{J\ kg}^{-1}\ \mathrm{K}^{-1}]$	750[g]
λ	$[\mathrm{J\ s}^{-1}\ \mathrm{m}^{-1}\ \mathrm{K}^{-1}]$	3[g,h]
ν		0.25[i]

Note. Superscripts denote the sources which are given at the bottom of the table. Values are from studies on olivine (90% forsterite). [a]Abramson et al. (1997). [b]Mao et al. (2015). [c]Hirth and Kohlstedt (2003). [d]Dixon and Durham (2018). [e]Hansen et al. (2019). [f]Breithaupt et al. (2023). [g]Osako et al. (2004). [h]Y. Zhang et al. (2019). [i]Gercek (2007). [j]Discussed in Section 2.4.

anomaly wrap around and approach it from the other side. The anomaly's semi-major axes are 375 and 125 m, respectively. Within the anomaly, we multiply the flow law pre-factors A_{dif} and A_{dis} by a weakening factor $\omega = 100$. As η_{LTP} is not that sensitive to A_{LTP}, we instead divide the back-stress σ_{b} by ω. The numerical resolution is 1,536 × 256 cells, yielding cell sizes of about 40 m in x-direction and 26–52 m in y-direction due to refinement, with the smallest cells in the center. All models use an olivine rheology (Table 1).

2.4. Reference Model

We consider a reference model at 20 GPa background pressure which approximates 600 km depth where the overwhelming majority of deep-focus earthquakes occurs (Frohlich, 2006; Zhan, 2020). When extrapolating flow laws to this depth, it is important to consider their activation volume (i.e., pressure-dependence). Especially for LTP, this value is highly controversial (Jain et al., 2017; Kawazoe et al., 2009), and we follow the approach of Breithaupt et al. (2023) who suggest that LTP has the same activation energy and volume as dislocation creep. The most established dislocation creep activation volume for olivine is 15 $\mathrm{cm}^3\ \mathrm{mol}^{-1}$ (Dixon & Durham, 2018; Hirth & Kohlstedt, 2003; Warren & Hansen, 2023), which coincides with the arithmetic mean between the minimum and maximum estimates for V_{LTP} (Jain et al., 2017; Kawazoe et al., 2009).

Furthermore, there may be additional pressure-dependencies in σ_{L} (Hansen et al., 2019; Proietti et al., 2016) and σ_{b} (Hansen et al., 2019). Proietti et al. (2016) suggest a hardening of 0.09 GPa^{-1} for σ_{L}, and Hansen et al. (2019) suggest that σ_{b} is as pressure sensitive as the elastic constants, with a hardening of 0.02 GPa^{-1} (Abramson et al., 1997; Mao et al., 2015). Figure 2 shows how τ_{LTP} evolves with increasing temperature and how it is affected by the hardening of σ_{L} and σ_{b}. Increasing σ_{L} affects the low temperature, and σ_{b} the high temperature branch of the flow law. σ_{L} and σ_{b} are adjusted to 20 GPa, considering that the experiments of Hansen et al. (2019) were conducted at about 6.5 GPa.

$$\sigma_{\mathrm{L,hard}} = \sigma_{\mathrm{L}} \frac{1 + P_0 \beta_{\mathrm{L}}}{1 + P_{\mathrm{H}} \beta_{\mathrm{L}}}, \tag{22}$$

$$\sigma_{\mathrm{b,hard}} = \sigma_{\mathrm{b}} \frac{1 + P_0 \beta_{\mathrm{b}}}{1 + P_{\mathrm{H}} \beta_{\mathrm{b}}}, \tag{23}$$

where $\beta_{\mathrm{L}} = 0.09\ \mathrm{GPa}^{-1}$, $\beta_{\mathrm{b}} = 0.02\ \mathrm{GPa}^{-1}$, and $P_{\mathrm{H}} = 6.5$ GPa. For simplicity, we also use P_0 for the viscosity calculations (Equations 14–17). The effects of this simplification and numerical parameters such as resolution are discussed in Text S1 and Figures S1, S2 in Supporting Information S1.

Another poorly constrained parameter is the grain size at depth which can only be inferred from rheological behavior (Behn et al., 2009), stress state (Karato, 1984), seismic velocities (Faul & Jackson, 2005), and growth kinetics (Riedel & Karato, 1997), all of which depend on other unknowns. Whereas the grain size in the upper mantle may be on the order of mm (Behn et al., 2009), it may be reduced to 10–100 µm in areas of deformation (Wada et al., 2011). The cold core of a subducting slab might have even lower grain size as it is expected to be characterized by high stress and low grain growth rates during deformation (Ito & Sato, 1991; Karato, 1984). Based on this, and to consider the potential contribution of grain size reduction, we choose a grain size of 1 µm. All parameters are given in Table 1. Decreasing the grain size from 10 to 1 µm has a similar effect as adjusting σ_{L} to 20 GPa of pressure, increasing the LTP stress by a few hundred MPa at low temperatures (Figure 2).

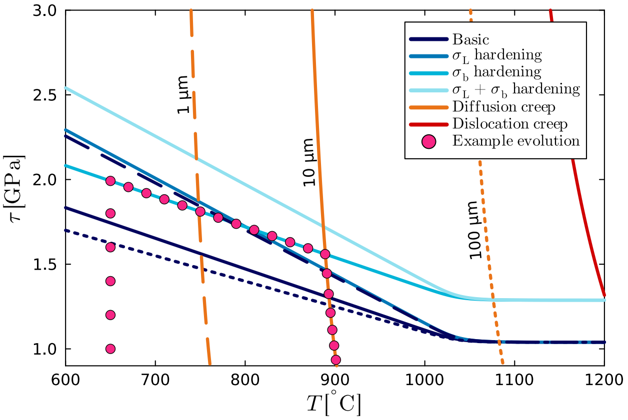

Figure 2. Deviatoric stress as a function of temperature for different low-temperature plasticity (LTP) flow law parameters and grain sizes. LTP in blues, diffusion creep in orange, and dislocation creep in red. Dashed lines represent $d = 1$ μm, solid lines $d = 10$ μm, and dotted lines $d = 100$ μm. Magenta dots outline the theoretical evolution (starting in the lower left) of a zero-dimensional model that is loaded elastically, then deforms by LTP, heats up as a consequence of viscous dissipation, and eventually transitions into diffusion creep. Calculated for $\dot{\varepsilon}_{\mathrm{bg}} = 2 \times 10^{-13}\ \mathrm{s}^{-1}$.

2.5. Parameter Variation

1D models of thermal runaway have demonstrated that the stress and temperature conditions at the transition from LTP to diffusion or dislocation creep are critical for the subsequent relaxation (Spang et al., 2024). The ratio of stored elastic energy to thermal energy is given by

$$\frac{U_{\mathrm{el}}}{U_{\mathrm{th}}} = \frac{\tau_{\mathrm{t}}^2}{T_{\mathrm{t}}} \frac{L}{2\, G\, f_{\mathrm{an}}\, \rho\, C_p\, h}, \tag{24}$$

where U_{el} and U_{th} are elastic and thermal energy respectively, τ_{t} and T_{t} are the transition stress and temperature, L is the size of the system, h the size of the anomaly, and f_{an} a factor describing its shape and magnitude (Spang et al., 2024). The larger the ratio, the more likely and potent is thermal runaway.

As the uncertain parameters discussed in Section 2.4 (grain size, pressure dependencies of LTP) can shift the conditions when LTP transitions into diffusion or dislocation creep, we investigate different combinations of these parameters. We test 3 grain sizes (1 μm, 10 μm, 100 μm), without any hardening, with σ_{L}-hardening, with σ_{b}-hardening, and both for a total 12 of models. Another eight models with different activation volumes help us cover the parameter space more thoroughly. All models are listed in Table S1 in Supporting Information S1.

3. Results

3.1. Reference Model

In Figure 3 and Section 3.1.1, we show the temporal evolution of deviatoric stress, velocity, and pressure in the reference model. In Figures 4 and 5 and Section 3.1.2, we focus on the processes taking place at the rupture tip.

3.1.1. Temporal Evolution

Initially, the deviatoric stress linearly and homogeneously increases in the entire domain, and the velocity field follows a linear vertical gradient (Figure 3a). Once the LTP-limit is reached, stress concentrations develop at the tips of the anomaly. A shear zone governed by LTP develops around the anomaly, localizing deformation into the center (Figure 3b). Temperature is slowly increasing during this time (Figure 3g).

Eventually, temperature in the tips of the anomaly is high enough for diffusion creep to become the dominant deformation mechanism there. This is accompanied by strong localization, and a second, much more localized shear zone starts to propagate across the model domain (Figure 3c, purple area in stress field). Inside this shear zone, stress drops by more than 1 GPa, and velocities are consistent with accelerated creep $\left(\sim 10^{-6}\ \mathrm{m\ s^{-1}}\right)$. As this ductile rupture propagates, stress in the surrounding host rock is also relaxed progressively. The ductile rupture accelerates, entering the seismic regime $\left(\sim 10^{-3}\ \mathrm{m\ s^{-1}}\right)$ after a few km. The rupture tips are surrounded by pressure anomalies of about 1.5 GPa (positive on the left in propagation direction, and negative on the right, Figure 3d).

The ruptures connect as the two rupture tips approach each other across the periodic boundary conditions. Slip velocities increase by another order of magnitude, and the opposing pressure anomalies vanish (Figure 3e). This moment coincides with the peak in temperature at around 1,800°C (Figure 3g). As deviatoric stress approaches zero in the entire domain, velocities delocalize and return to an AC-level across the entire shear zone (Figure 3f). In this final stage, the model behaves similarly to a 1D model as the shear zone extends through the entire domain, effectively dividing it into two decoupled blocks.

Maximum velocity $v_{\max}$ and minimum viscosity $\eta_{\min}$ occur in the tip of the ductile rupture and are roughly inversely correlated (Figure 3h). At the beginning of thermal runaway, $\eta_{\min}$ decreases by about 10 orders of magnitude while $v_{\max}$ increases by about 5. Both trends flatten out once $\eta_{\min}$ approaches the regularization

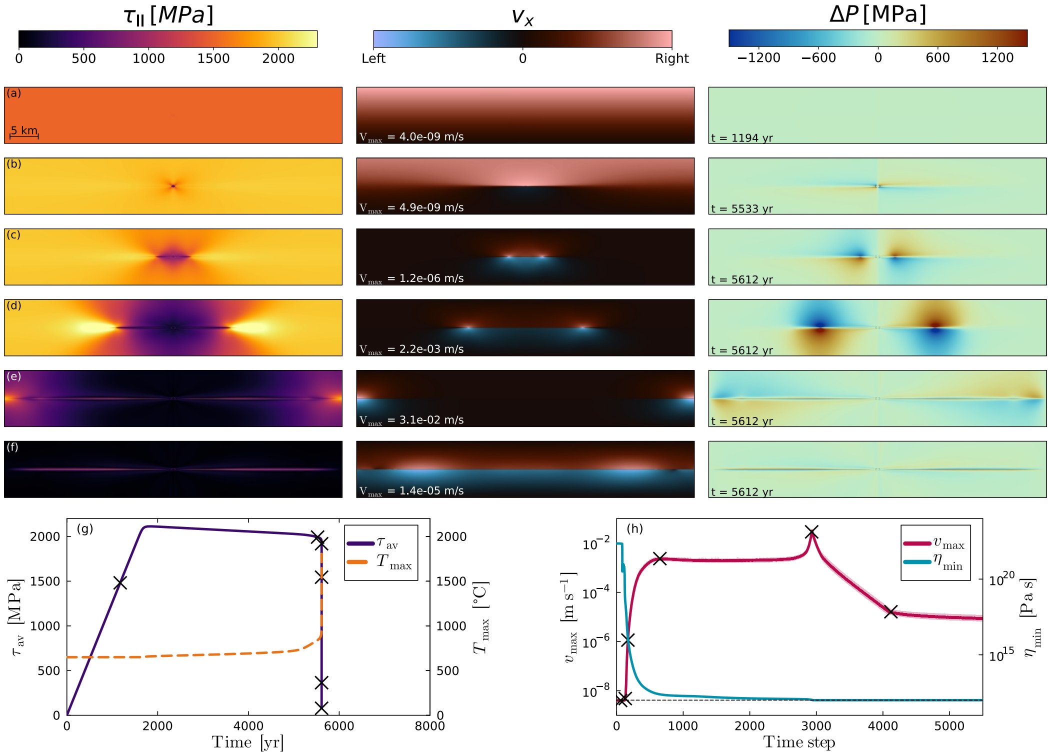

Figure 3. Temporal evolution of reference model. Colorplots show stress, velocity, and pressure anomaly field at six different time steps. (a) Elastic loading stage. (b) Low-temperature plasticity shear zone starts forming in the center. (c) Thermal runaway-driven rupture starts to propagate. (d) Propagation continues, and velocities reach seismic values. (e) Rupture tips connect across periodic boundary conditions. (f) Most stress has been released and deformation delocalizes. (g) Average deviatoric stress (τ_{av}) and maximum temperature ($T_{\max}$). Six black crosses represent the six stages shown in panels (a–f). (h) Maximum horizontal velocity ($v_{\max}$) and minimum viscosity ($\eta_{\min}$). Note that we plot time step instead of time here as the majority of velocity and viscosity evolution takes place during the stress drop in panel (g). Black dashed line shows η_{reg}. Note that $v_{\max}$ shows some high frequency oscillations and was smoothed with a moving average of width 11.

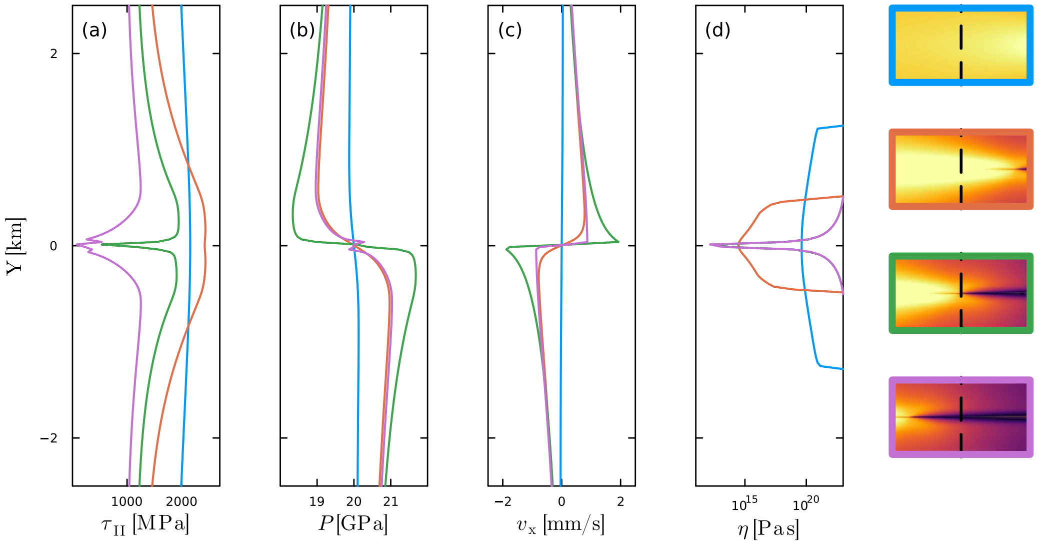

Figure 4. Vertical profiles through the domain where colors indicate different times. Column on the right is a legend that shows where the rupture is in regards to the profile for each line. (a) Deviatoric stress. (b) Pressure. (c) Horizontal velocity. (d) Viscosity. Note that the green curve is covered by the purple one in this plot.

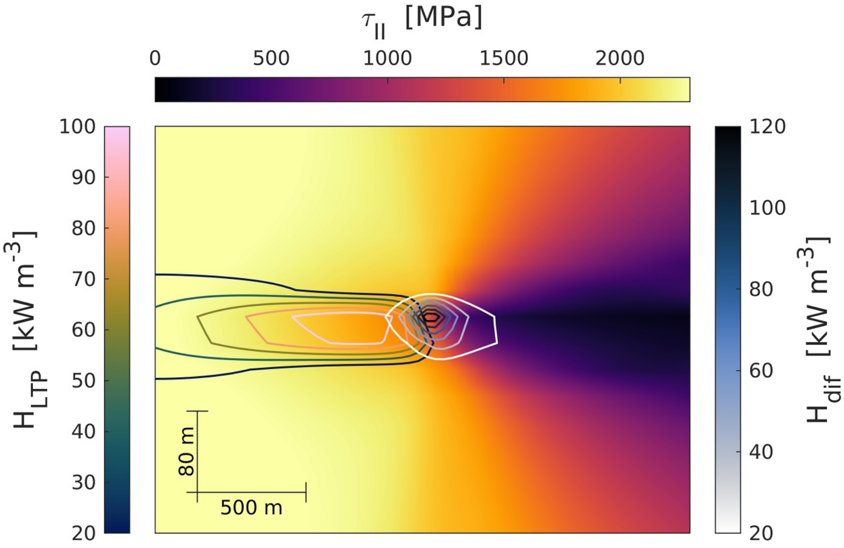

Figure 5. Zoom on the rupture tip. Background colors indicate deviatoric stress τ_{II} in MPa. Set of contour lines to the left show viscous dissipation from low-temperature plasticity, and contour lines to the right show viscous dissipation from diffusion creep. One contour every 20 kW m^{-3}.

viscosity η_{reg}. v_{max} shows some high frequency oscillations which is also a typical and hard to resolve problem in numerical models of brittle earthquakes, and a posteriori smoothing is commonly applied (Moczo et al., 2014).

3.1.2. Rupture Tip

In Figure 4, we show vertical profiles of deviatoric stress τ_{II}, pressure P, horizontal velocity v_x, and viscosity η at different time steps to illustrate how these parameters evolve as the ductile rupture tip passes through.

When the thermal runaway front is still far away (blue), the stress field is homogeneous along the profile (Figure 4a). As the tip of the thermal runaway rupture approaches (orange), stress starts to decrease in the host rock, but slightly increases in the center due to the high-stress area ahead of the tip. When the tip reaches the profile location (green), stress drops significantly in the center but remains higher just outside the rupture. Once the rupture tip has passed the profile (purple), stress has dropped by about one GPa along the entire profile and two GPa in the center.

In Figures 4b and 4c, we show the same profiles for pressure P and horizontal velocity v_x. Pressure changes by about 1.5 GPa in both directions on either side of the rupture as it passes, but returns to a more homogeneous state afterward. Velocity is high in the center as the tip passes, but unlike pressure, the respective peaks only decrease, but do not disappear after the tip has passed.

In Figure 4d, we show viscosity η. The orange line indicates that the LTP-dominated high stress zone ahead of the tip is a few hundred meters wide whereas the diffusion creep-dominated ductile rupture is more localized (purple line). The material in the ductile rupture is about 10 orders of magnitude weaker than the host rock due to the temperature increase.

The overwhelming majority of viscous dissipation occurs at the rupture tip and in an area of about 1 km ahead of it (Figure 5). Diffusion creep dominates at the ductile rupture tip, and LTP dominates in the high-stress region ahead of the rupture. The dissipation maximum is at the rupture tip where stress is still moderate and strain rates are high. During runaway, the heat generation reaches more than 100 kW m^{-3}.

3.2. Parameter Sensitivity

Depending on the employed rheological parameters (Table S1 in Supporting Information S1), stress relaxation can evolve differently to the reference model. In Figure 6, we illustrate the stress evolution in three characteristic models. Roman numerals denote the different stages.

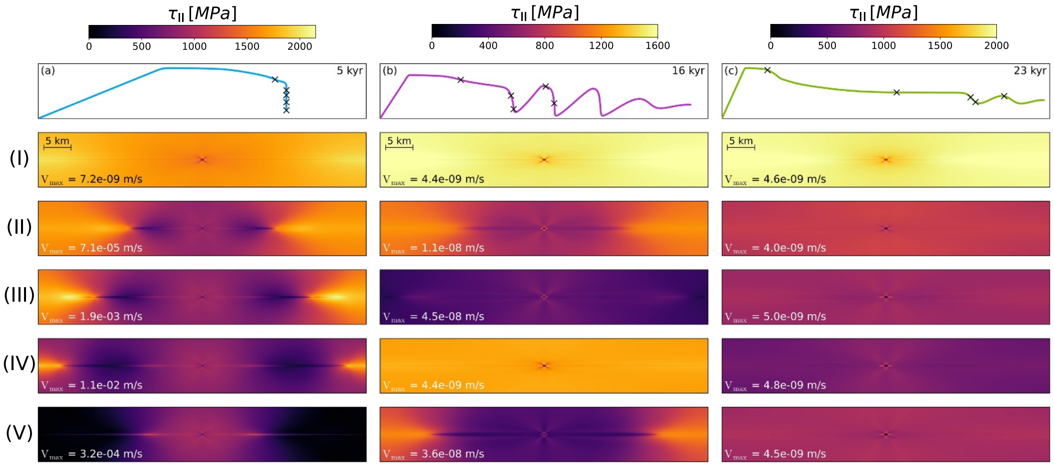

Figure 6. Temporal evolution of three other models exhibiting different behavior. Each column is one model and the first row shows the temporal evolution of average deviatoric stress. Length of *x*-axis is given in the top-right corner. Crosses indicate the timing of the five snapshots below, numbered by roman numerals. Snapshots show deviatoric stress field in MPa, and maximum velocity is indicated in the corners. (a) $d = 10$ μm, σ_L-hardening, σ_b-hardening. (b) $d = 10$ μm. (c) $d = 100$ μm, σ_L-hardening.

For the model in Figure 6a, we use a larger grain size (10 μm) and adjust σ_L and σ_b to the pressure according to Equations 22 and 23. Initially, an LTP shear zone develops over the entire horizontal extent of the model (I) before a more localized diffusion creep front moves through the domain at speeds in line with accelerated creep (II). During this stage, stress in the model center is only partly released, unlike in the reference model (Figure 3d). Only further away from the center, slip velocities reach the seismic window, and stress is fully released in the rupture tip (black areas in III and IV). After the rupture fronts have united, propagation resumes inwards to also release the stress in the model center (V).

The model in Figure 6b (grain size of 10 μm, but no hardening of σ_L and σ_b) shows the same initial, LTP-dominated stage (I), before a diffusion creep front unloads most of the stress (II, III). In this case, the velocities are at the lower end of the AC spectrum. The result is less temperature increase and less thermal weakening along the rupture path, and stresses can build back up (IV). This is followed by multiple cycles of stress release (V), cooling, and rebuild of stress.

Relaxation in the model in Figure 6c (grain size of 100 μm, hardening of σ_L) is so slow that velocities barely exceed the far-field deformation. The model exhibits the aforementioned LTP-driven period which lasts thousands of years in this case (I, II). Eventually, a diffusion creep-dominated shear zone propagates through the model and unloads stress by about 300 MPa over a thousand years, but slip velocities do not increase (III, IV). Similarly to the model in Figure 6b, stress recovers (V) before another, even less pronounced unloading phase.

Among the 20 tested parameter combinations (see Section 2.5, Table S1 in Supporting Information S1), we observe four different types of behavior. (a) Seismic slip velocities $\left(>1\ \mathrm{mm\ s^{-1}}\right)$ are reached within a few km from the anomaly (Figure 3, orange in Figure 7) with local heating rates of up to 0.5 K $\mathrm{s^{-1}}$. (b) AC-type ruptures that can reach seismic velocities when two ruptures connect (Figure 6a, blue in Figure 7). Local heating rates can exceed 1 K $\mathrm{d^{-1}}$. (c) Repeating events of localized slip that is up to two order of magnitude faster than the background deformation rate (Figure 6b, purple in Figure 7). During these events, temperatures can locally rise by 100 K $\mathrm{yr^{-1}}$. Afterward, the shear zone cools, strengthens, and stress builds back up for the next event. (d) Continuous slow deformation without significant changes in velocity or temperature (Figure 6c, green in Figure 7). Even in the latter case, a shear zone forms and stress can decrease by a few hundred MPa. The temporal evolution of mean stress, maximum temperature, and maximum velocity of all models are shown in Figure 7.

In Figure 7a, we show the stress and temperature conditions where the deformation is expected to switch from LTP to diffusion creep for all our models. This reveals that similar model behavior correlates with similar transition conditions. Contouring Figure 7a with the ratio of elastic to thermal energy according to Equation 24

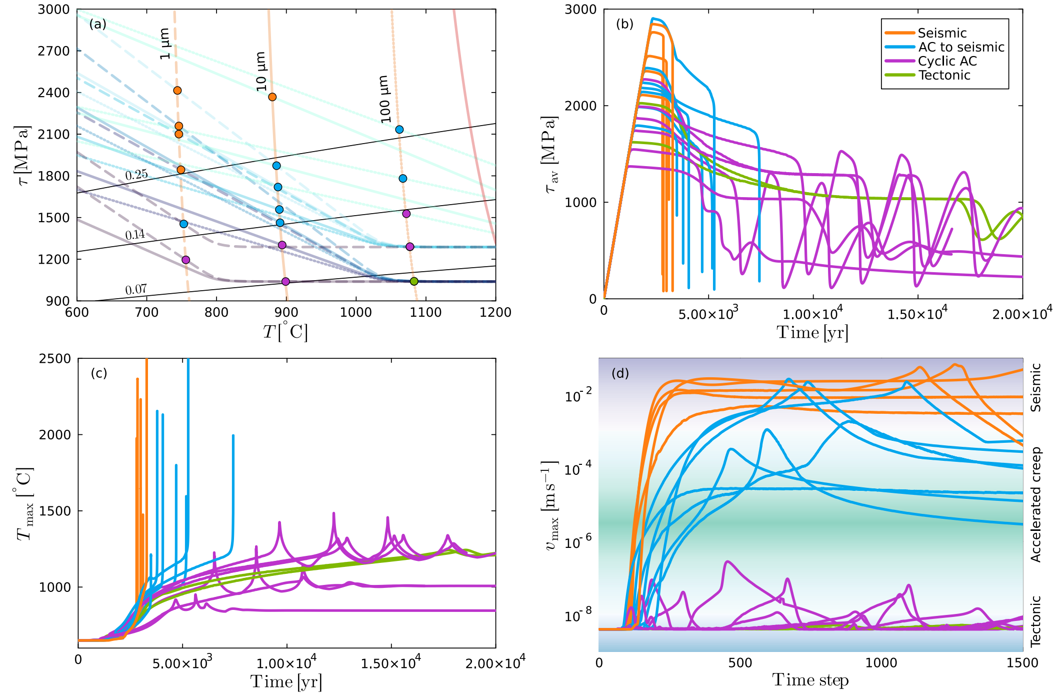

Figure 7. Model sensitivity to rheological parameters. (a) Analogous to Figure 2. Semi-transparent lines indicate different flow law parameters. Colored dots show expected transition conditions to diffusion creep for 20 models (two pairs on the right plot on top of another). Colors group models with similar behavior (see legend in b). Black lines are contours for U_{el}/U_{th} that separate the different behaviors. (b–d) Temporal evolution of 20 models grouped with the same color scheme used in panel (a). (b) Mean deviatoric stress. (c) Maximum temperature. (d) Maximum velocity. Background color shading indicates seismic, AC, and plate tectonics velocity regime from top to bottom. Note that the *x*-axis is time step and not time.

(Spang et al., 2024), allows us to separate the individual groups of models from another. For larger U_{el}/U_{th}, thermal runaway is more likely, and stress drops, temperature rises, and maximum velocities are larger.

3.3. Induced Brittle Failure

The tips of the ductile ruptures are flanked by zones of increased and decreased pressure of up to about 1.5 GPa (Figure 3). Close to the brittle-ductile transition, pressure variations can cause deformation to shift from the ductile to the brittle regime. In Figure 8, we show the evolution of a model at conditions just below the brittle-ductile transition zone. At 600°C and 2.3 GPa lithostatic pressure, LTP limits deviatoric stresses to about 1 GPa. Considering Drucker-Prager plasticity (Drucker & Prager, 1952), the brittle limit is given by $\tau_{br} = P\sin(\phi) + c\cos(\phi)$. With negligible cohesion (c) and a typical friction angle (ϕ) of 30°, the brittle strength (τ_{br}) is 1.15 GPa.

At a deviatoric stress of about 1 GPa, our models produce ductile ruptures in line with AC, but they still create transient pressure anomalies of several hundred MPa (Figure 8). This is enough to locally lower the brittle strength of the rocks sufficiently to cause brittle failure. Black outlines in Figure 8 show the areas where τ_{II} exceeds τ_{br}. These areas are located in front and to the right of the rupture tip in propagation direction. They are up to a few km in diameter and move with the propagating rupture. Note that we do not explicitly account for brittle plasticity in the rheology of the model but only analyze the stress fields created in the visco-elastic experiments.

4. Discussion

4.1. Transient Ductile Rupture Propagation

Our models demonstrate that thermal runaway can nucleate on perturbations and lead to the formation of highly localized shear zones which accommodate slip that is orders of magnitude faster than the far-field deformation. These shear zones can propagate through previously intact host rock without a pre-existing fault surface or weak

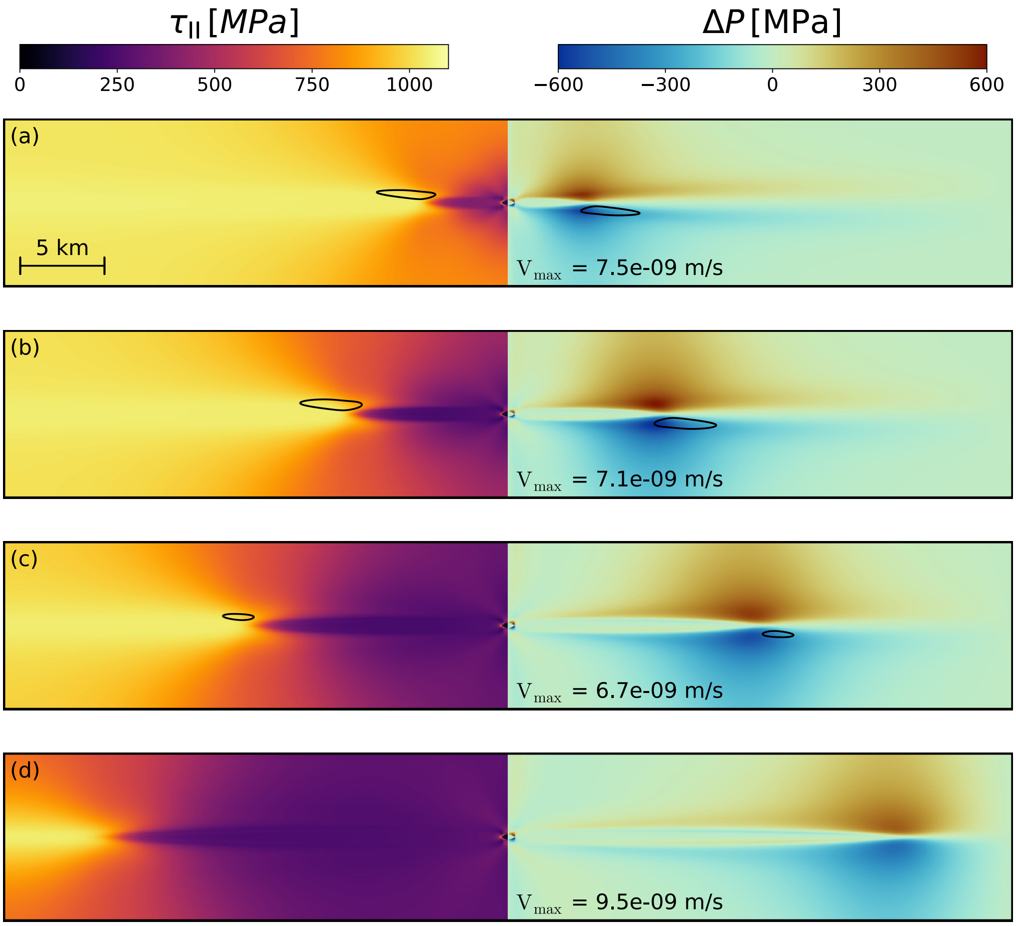

Figure 8. Temporal evolution of model at 2.3 GPa. Left column shows deviatoric stress in MPa and right column shows pressure anomaly in MPa. Each column only shows one side of the symmetric model. Black outlines show the area where the deviatoric stress exceeds the brittle limit. Changed parameters in comparison to reference model: $T_0 = 600\ ^\circ\mathrm{C}$, $P_0 = 2.3$ GPa, $d = 10$ µm, $G = 70$ GPa, $C_p = 800\ \mathrm{J\ kg^{-1}\ K^{-1}}$, $\omega = 10$.

layer. The unification of two rupture fronts causes slip velocity to peak (Figure 3h). Viscous dissipation is highest in the rupture tips where stress and strain rate are both large (Figure 5). The rupture tips are flanked by opposing pressure anomalies that can reach magnitudes of more than one GPa. Similar structures are found in models of brittle earthquakes (Cocco & Rice, 2002; Di Toro et al., 2005; Reches & Lockner, 1994; Thomas et al., 2017).

4.2. Parameter Sensitivity

Depending on the employed LTP parameters and grain size, our models reach different stress and temperature conditions before transitioning into diffusion creep-dominated relaxation. These conditions can be non-dimensionalized and summarized by the ratio of elastic to thermal energy $U_{\mathrm{el}}/U_{\mathrm{th}}$ (Equation 24, Spang et al., 2024). If this ratio is sufficiently large, thermal runaway can cause ductile ruptures that reach velocities $>1\ \mathrm{mm\ s^{-1}}$. If the ratio is small, shear zones still form, but velocities do not exceed background deformation rates by more than a factor of two (Figure 7).

Our parameter study aligns well with the 1D scaling law of Spang et al. (2024). It is thus to be expected that size of the deforming area, heat capacity, density, and shear modulus can also influence the occurrence of runaway and the type of rupture propagation. Testing all of these additional parameters comprehensively is computationally too expensive in 2D, but we present a reduced study in Text S3 and Figure S3 in Supporting Information S1. The results support the statement above.

Strain rate and thermal conductivity play a different role than the other parameters. They have no influence on the maximum slip velocities reached during runaway, but, if perturbed enough (e.g., one order of magnitude lower strain rate), they can inhibit the initiation of runaway (Figures S3c, S3d, and Text S3.2 in Supporting Information S1).

The properties of the anomaly do not play a significant role (Figures S3e, S3f, and Text S3.3 in Supporting Information S1) as the runaway largely occurs in the unperturbed host rock. It is possible to reproduce the same runaway event by only lowering the grain size in the anomaly instead of perturbing the flow law parameters.

4.3. Arresting Propagation

Our models do not show how ductile ruptures are halted. In the rate and state friction parameterization, the empirically constrained state parameter can lead to strengthening which ultimately arrests the propagating fault (Dieterich, 1979). As there are no experiments on thermal runaway, our rheology contains no such strengthening mechanism. However, as suggested by the ratio $U_{\mathrm{el}}/U_{\mathrm{th}}$ and the decay of slip velocity in 1D models (Braeck et al., 2009; Spang et al., 2024; Thielmann et al., 2015) as well as after the unification of two rupture fronts in 2D (Figure 3h), thermal runaway requires stress to be large enough to keep deformation localized. We propose that ductile ruptures are arrested when they enter areas that are at lower stress. Increase of background temperature, decrease of background deformation, or weaker material through heterogeneities all result in low stress and could therefore arrest ductile ruptures.

4.4. Comparison to 1D Models

We mainly compare our results to those of Spang et al. (2024) as we use the same rheological model and boundary conditions. However, most similarities also apply to other 1D studies (e.g., Braeck et al., 2009; John et al., 2009; Ogawa, 1987; Thielmann, 2018; Thielmann et al., 2015). The temporal evolution of mean deviatoric stress, maximum temperature, minimum viscosity, and maximum slip velocity are very similar to 1D models of thermal runaway (Figures 3g and 3h). Vertical 1D profiles through our 2D models also exhibit similar velocity and viscosity distributions to 1D models (Figures 4c and 4d).

In our 2D models, peak temperatures, strain rates, and velocities are all lower than in 1D models. This likely stems from the fact that a weak inclusion extends infinitely in 1D models, whereas the rupture needs to propagate through intact host rock in 2D. With the periodic boundary conditions that we apply, the 2D model becomes mechanically equivalent with the 1D model once the rupture tips connect and effectively cut the model into an upper and lower half. This coincides with a significant peak in velocities. At this point, however, a large part of the elastically stored stress has already been released, and consequently velocities and temperatures do not reach the levels of 1D models.

The largest difference between 1D and 2D models is that viscous dissipation varies strongly in propagation direction of the rupture (Figure 5). This results in a large variation of viscosity, stress and strain rate along the dimension that is not present in 1D models. Thus, it is much harder to predict the stress and temperature at which stress release starts. Despite this complication, the dimensionless ratio of elastic and thermal energy in the system $U_{\mathrm{el}}/U_{\mathrm{th}}$, derived from 1D models (Spang et al., 2024) still has strong predictive power in 2D (Figure 7a). Finally, the area of highest dissipation rate moves through the 2D model domain, while in 1D it stays in the same location for the entire runaway. This is another reason why maximum temperatures in 2D models are lower and more reasonable than in 1D.

4.5. Numerical Limitations

Our models cannot reliably estimate the maximum slip velocity and temperature reached during strong runaway. As discussed in numerous previous studies, fast deformation and elasticity commonly lead to localization onto a single grid cell and resolution-dependent results (De Borst et al., 1993; Iordache & Willam, 1998; Jacquey et al., 2021). This problem can be mitigated by the introduction of a viscosity regularization as used here (see Section 2.2.2), but the regularization will still provide a soft, artificial upper velocity limit in this case (Figure S1b in Supporting Information S1, Goudarzi et al., 2023; Spang et al., 2024). A regularization viscosity of 10^{12} Pa s is low enough to allow models to reach seismic velocities (Figures 3 and 6). The inclusion of inertial terms and advection are probably necessary for a better estimation of upper limit velocities. Exploring different regularization approaches (e.g., Duretz et al., 2023; Goudarzi et al., 2023) might also alleviate these issues.

Other uncertainties stem from the fact that our model does not account for the effects of melting on the rheology and energy budget of the system. It is unclear whether the expected melt-related weakening would outweigh the energy lost to latent heat. So this simplification could lead to an over- or underestimation of velocity and temperature. Finally, heat loss due to advection, in particular injection veins (Andersen et al., 2014) could limit temperature increase, but only after crossing the melting point.

Our models are still missing one spatial dimension compared to reality. However, the mechanical difference between 2D and 3D models is considerably smaller than between 1D and 2D. Li et al. (2022) investigated 0D to 3D brittle rupture models and demonstrated that slip velocities reduce by a factor of about two when adding the third spatial dimension.

4.6. Implications for Deep Earthquakes

Our 2D models demonstrate that thermal runaway is a viable mechanism to cause transient propagation of ductile ruptures under conditions appropriate for the mantle transition zone. Depending on the stress-temperature-conditions, these ruptures can reach aseismic slip velocities in line with SSEs or seismic slip velocities comparable to brittle earthquakes (Bürgmann, 2018; Kirkpatrick et al., 2021; Weng & Ampuero, 2022). SSEs have never been reported at such depth, but this might be due to the difficulty of detecting them (Behr & Bürgmann, 2021; Nishikawa et al., 2023; Schwartz & Rokosky, 2007).

Whether the required conditions for earthquake-like slip can be reached in nature depends on poorly constrained parameters like the pressure-dependency of LTP and the grain size of cold slab cores. Within the current estimates, they can be reached, making thermal runaway a potential mechanism for deep-focus earthquakes. Given the scarcity of deep-focus earthquakes (Frohlich, 2006; Zhan, 2020), it is likely that only a few sections of slabs reach these conditions.

The models that only reach large velocities once two rupture tips approach each other (Figure 6a) suggest that deep-focus earthquakes can also be caused by multiple runaway-driven accelerated creep events that unite. This would be analogous to the proposal that shallow SSEs can trigger brittle earthquakes (e.g., Obara & Kato, 2016; Segall & Bradley, 2012; Uchida et al., 2016).

As suggested by 1D models (Spang et al., 2024), thermal runaway is unlikely to initiate on its own at the grain scale. Instead, it is more likely to be part of a dual-mechanism process as suggested by previous studies (e.g., Bezada & Humphreys, 2012; McGuire et al., 1997; Zhan, 2020). For deep-focus earthquakes, an area of metastable olivine could transform to fine-grained spinel which acts as a rheological anomaly that can initiate thermal runaway (e.g., Gasc et al., 2022; Green & Burnley, 1989; Kirby, 1987; Rubie & Ross, 1994; Schubnel et al., 2013). Our models demonstrate that thermal runaway can, once initiated, propagate tens of kilometers to create a large rupture area. In Figure S3f in Supporting Information S1, we show that an area of reduced grain size can initiate the same ductile rupture as the flow law perturbations we used.

Our models show that high stresses are necessary for fast, thermal runaway-driven ruptures (Figure 7). This finding is consistent with the low number of earthquakes between 200 and 500 km depth and the much larger number of events at around 600 km depth (Frohlich, 2006; Zhan, 2020). There are two requirements for large stress: (a) relatively fast deformation and (b) a strong material to sustain the stress; both of which are met below 500 km depth. The resistance of the 660 km discontinuity deflects the tip of the subducting slab while the up-dip portions are pushed downwards by the 410 km discontinuity (Billen, 2020; Fukao et al., 2001; Tao & O'Connell, 1993; Turcotte & Schubert, 2002; Zhan, 2020). At the same time, the pressure-dependent flow-laws predict a higher strength at large pressure (Equations 14–17). Ductile earthquakes at shallower depth probably require additional stress sources like dehydration reactions (e.g., Ferrand et al., 2017; Hacker et al., 2003; Porkoláb et al., 2025; Raleigh & Paterson, 1965) or focused deformation around inclusions (Toffol et al., 2022).

The pressure field induced by the ductile rupture (Figure 3) is consistent with the distribution of injection veins around pseudotachylytes. Field observations (Di Toro et al., 2005) and conceptual models (Griffith et al., 2012) show that these predominantly form on the right side of the rupture in propagation direction which coincides with the negative pressure perturbation in our models. Furthermore, the magnitude of the pressure anomalies (~ 1 GPa) is within estimates of required pressure difference to open injection veins (0.1–10 GPa, Rowe et al., 2012).

The majority of deep earthquake stress drop estimates, derived from seismological observations, range from 5 to 100 MPa (Frohlich, 2006). However, Prieto et al. (2013) argue that these estimates could also be much larger if the low rupture velocity of ductile earthquakes was considered. Minimum estimates based on the required energy for the production of pseudotachylytes range from 220 to 580 MPa (Andersen et al., 2008). Obata and Karato (1995) suggest 300–600 MPa, based on dislocation density and grain size. Stress drops in our models are larger and range from 1 to 2.5 GPa. However, it is unclear whether the whole relaxation can be considered as only a part of the stress release occurs during the velocity peak. A more robust comparison to seismic observations would require a wave propagation model which uses the results of our models as input.

The solidus of mantle rocks is about 2,100°C at 20 GPa (Miller et al., 1991). Maximum temperatures in most of our fast-slipping models exceed this value (Figure 7c, not all models reached their peak yet). As discussed in Section 4.5, our models cannot reliably estimate maximum temperature. But considering the regularization, the values are likely to be underestimations. It is therefore likely that a ductile rupture will reach the temperatures necessary to locally melt the host rock and produce pseudotachylytes.

4.7. Implications for Induced Brittle Failure

Slow slip events have been considered as drivers of brittle earthquake swarms (Collot et al., 2017; Fukuda, 2018; Lohman & McGuire, 2007; Nishikawa et al., 2023; Vidale & Shearer, 2006). Studies propose that SSEs transfer stress from one area to another where the stress increase leads to brittle failure (Fukuda, 2018; Vidale & Shearer, 2006). While these observations were made at significantly shallower areas of the lithosphere, where thermal runaway is unlikely to function, they show parallels to our results (Figure 8).

The low-pressure (2.3 GPa) models presented in Section 3.3 demonstrate that aseismic, runaway-driven, ductile slip can induce pressure changes that locally suppress the brittle strength of the host rock. In the lithospheric mantle, within a few hundred MPa below the brittle-ductile transition, this effect is large enough to trigger brittle failure in an otherwise ductile host rock. Unlike the inferred triggering by stress transfer (Fukuda, 2018; Vidale & Shearer, 2006), these small brittle earthquakes would predominantly be triggered by a reduction of the brittle strength due to a local pressure decrease.

5. Conclusions

In this study, we use two-dimensional, thermomechanical, simple-shear models with a Maxwell rheology including, elasticity, diffusion creep, dislocation creep, and LTP. The models capture the nucleation and transient propagation of highly localized, thermal runaway-driven, ductile ruptures. These ruptures reach a wide range of slip velocities between the magnitudes of plate tectonics and seismic events. The intensity of runaway and magnitude of velocity depend on the stress- and temperature-conditions when deformation transitions from LTP to diffusion creep. The propagating rupture tips perturb the stress state of the surrounding host rock by hundreds of MPa to a few GPa.

Applying our models to mantle transition zone conditions confirms thermal runaway as a potential driver of deep-focus earthquakes. Once initiated at a small perturbation such as an area of post-transformational spinel, thermal runaway can facilitate ductile ruptures of several tens of kilometers in the cold core of subducting slabs. Whether the slab can reach the required stress for seismic slip velocities is within the uncertainty of rheological flaw laws and grain size estimates. The need for large stress offers an explanation for the scarcity of deep earthquakes between 200 and 500 km depth and their abundance at 600 km depth.

Applying our models to the brittle-ductile transition zone shows that thermal runaway can drive accelerated creep events in this depth range. These events are significantly slower than deep earthquakes, but they perturb the pressure field around the ductile rupture tip enough, to induce brittle failure in an otherwise ductile host rock. This has potential implications for the mechanical link between SSEs and swarms of brittle earthquakes which are commonly detected in close proximity of another.

Data Availability Statement

Figures were created with Plots.jl, version 1.40.8 (Breloff, 2024), available on zenodo at https://zenodo.org/records/10959005 and MATLAB version R2022a (Figure 5, MathWorks Inc, 2022). The code we developed and used for this study (Spang et al., 2025) is available on zenodo at https://doi.org/10.5281/zenodo.14719483. It uses the package GeoParams.jl (Kaus et al., 2023) available on Zenodo at https://doi.org/10.5281/zenodo.10050339.

Acknowledgments
We thank Mark Behn, Pietro Sternai, Julian Mecklenburgh and one anonymous reviewer for their encouraging and constructive comments. A.S. and M.T. were funded by the DFG Grant TH 2076/8-1 awarded to M.T. This research has been supported by the Swiss University Conference and the Swiss Council of Federal Institutes of Technology through the Platform for Advanced Scientific Computing (PASC), obtained via the PASC project GPU4GEO. The authors gratefully acknowledge the scientific support and HPC resources provided by the Erlangen National High Performance Computing Center (NHR@FAU) of the Friedrich-Alexander-Universität Erlangen-Nürnberg (FAU). The hardware is funded by the German Research Foundation (DFG). Open Access funding enabled and organized by Projekt DEAL.

References

Abramson, E., Brown, J., Slutsky, L., & Zaug, J. (1997). The elastic constants of San Carlos olivine to 17 GPa. *Journal of Geophysical Research: Solid Earth*, *102*(B6), 12253–12263. https://doi.org/10.1029/97jb00682

Andersen, T. B., Austrheim, H., Deseta, N., Silkoset, P., & Ashwal, L. D. (2014). Large subduction earthquakes along the fossil Moho in Alpine Corsica. *Geology*, *42*(5), 395–398. https://doi.org/10.1130/g35345.1

Andersen, T. B., Mair, K., Austrheim, H., Podladchikov, Y. Y., & Vrijmoed, J. C. (2008). Stress release in exhumed intermediate and deep earthquakes determined from ultramafic pseudotachylyte. *Geology*, *36*(12), 995–998. https://doi.org/10.1130/g25230a.1

Antolovich, S. D., & Armstrong, R. W. (2014). Plastic strain localization in metals: Origins and consequences. *Progress in Materials Science*, *59*, 1–160. https://doi.org/10.1016/j.pmatsci.2013.06.001

Behn, M. D., Hirth, G., & Elsenbeck, J. R. II. (2009). Implications of grain size evolution on the seismic structure of the oceanic upper mantle. *Earth and Planetary Science Letters*, *282*(1–4), 178–189. https://doi.org/10.1016/j.epsl.2009.03.014

Behr, W. M., & Bürgmann, R. (2021). What's down there? The structures, materials and environment of deep-seated slow slip and tremor. *Philosophical Transactions of the Royal Society A*, *379*(2193), 20200218. https://doi.org/10.1098/rsta.2020.0218

Behr, W. M., Kotowski, A. J., & Ashley, K. T. (2018). Dehydration-induced rheological heterogeneity and the deep tremor source in warm subduction zones. *Geology*, *46*(5), 475–478. https://doi.org/10.1130/g40105.1

Bezada, M., & Humphreys, E. (2012). Contrasting rupture processes during the April 11, 2010 deep-focus earthquake beneath Granada, Spain. *Earth and Planetary Science Letters*, *353*, 38–46. https://doi.org/10.1016/j.epsl.2012.08.001

Billen, M. I. (2020). Deep slab seismicity limited by rate of deformation in the transition zone. *Science Advances*, *6*(22), eaaz7692. https://doi.org/10.1126/sciadv.aaz7692

Braeck, S., Podladchikov, Y. Y., & Medvedev, S. (2009). Spontaneous dissipation of elastic energy by self-localizing thermal runaway. *Physical Review E*, *80*(4), 046105. https://doi.org/10.1103/physreve.80.046105

Braun, J., Chéry, J., Poliakov, A., Mainprice, D., Vauchez, A., Tomassi, A., & Daignières, M. (1999). A simple parameterization of strain localization in the ductile regime due to grain size reduction: A case study for olivine. *Journal of Geophysical Research: Solid Earth*, *104*(B11), 25167–25181. https://doi.org/10.1029/1999jb900214

Breithaupt, T., Katz, R. F., Hansen, L. N., & Kumamoto, K. M. (2023). Dislocation theory of steady and transient creep of crystalline solids: Predictions for olivine. *Proceedings of the National Academy of Sciences*, *120*(8), e2203448120. https://doi.org/10.1073/pnas.2203448120

Breloff, T. (2024). Plots.jl [Software]. *Zenodo*. https://doi.org/10.5281/zenodo.13384570

Bürgmann, R. (2018). The geophysics, geology and mechanics of slow fault slip. *Earth and Planetary Science Letters*, *495*, 112–134. https://doi.org/10.1016/j.epsl.2018.04.062

Burnley, P. C., Green, H. W., & Prior, D. J. (1991). Faulting associated with the olivine to spinel transformation in Mg_2GeO_4 and its implications for deep-focus earthquakes. *Journal of Geophysical Research: Solid Earth*, *96*(B1), 425–443. https://doi.org/10.1029/90jb01937

Byerlee, J. (1978). Friction of rocks. In *Rock friction and earthquake prediction* (pp. 615–626). Birkhäuser.

Cocco, M., & Rice, J. R. (2002). Pore pressure and poroelasticity effects in Coulomb stress analysis of earthquake interactions. *Journal of Geophysical Research: Solid Earth*, *107*(B2), ESE-2. https://doi.org/10.1029/2000jb000138

Collot, J.-Y., Sanclemente, E., Nocquet, J.-M., Leprêtre, A., Ribodetti, A., Jarrin, P., et al. (2017). Subducted oceanic relief locks the shallow megathrust in central Ecuador. *Journal of Geophysical Research: Solid Earth*, *122*(5), 3286–3305. https://doi.org/10.1002/2016jb013849

De Borst, R., Sluys, L. J., Muhlhaus, H.-B., & Pamin, J. (1993). Fundamental issues in finite element analyses of localization of deformation. *Engineering Computations*, *10*(2), 99–121. https://doi.org/10.1108/eb023897

Desrues, J., Bésuelle, P., & Lewis, H. (2007). Strain localization in geomaterials. *Geological Society, London, Special Publications*, *289*(1), 47–73. https://doi.org/10.1144/sp289.4

Dieterich, J. H. (1979). Modeling of rock friction: 1. Experimental results and constitutive equations. *Journal of Geophysical Research: Solid Earth*, *84*(B5), 2161–2168. https://doi.org/10.1029/jb084ib05p02161

Di Toro, G., Nielsen, S., & Pennacchioni, G. (2005). Earthquake rupture dynamics frozen in exhumed ancient faults. *Nature*, *436*(7053), 1009–1012. https://doi.org/10.1038/nature03910

Dixon, N. A., & Durham, W. B. (2018). Measurement of activation volume for creep of dry olivine at upper-mantle conditions. *Journal of Geophysical Research: Solid Earth*, *123*(10), 8459–8473. https://doi.org/10.1029/2018jb015853

Drucker, D. C., & Prager, W. (1952). Soil mechanics and plastic analysis or limit design. *Quarterly of Applied Mathematics*, *10*(2), 157–165. https://doi.org/10.1090/qam/48291

Duretz, T., Räss, L., de Borst, R., & Hageman, T. (2023). A comparison of plasticity regularization approaches for geodynamic modeling. *Geochemistry, Geophysics, Geosystems*, *24*(7), e2022GC010675. https://doi.org/10.1029/2022gc010675

Duretz, T., Räss, L., Podladchikov, Y., & Schmalholz, S. (2019). Resolving thermomechanical coupling in two and three dimensions: Spontaneous strain localization owing to shear heating. *Geophysical Journal International*, *216*(1), 365–379. https://doi.org/10.1093/gji/ggy434

Duretz, T., Schmalholz, S., & Podladchikov, Y. (2015). Shear heating-induced strain localization across the scales. *Philosophical Magazine*, *95*(28–30), 3192–3207. https://doi.org/10.1080/14786435.2015.1054327

Fagereng, Å., Hillary, G. W., & Diener, J. F. (2014). Brittle-viscous deformation, slow slip, and tremor. *Geophysical Research Letters*, *41*(12), 4159–4167. https://doi.org/10.1002/2014gl060433

Faul, U. H., & Jackson, I. (2005). The seismological signature of temperature and grain size variations in the upper mantle. *Earth and Planetary Science Letters*, *234*(1–2), 119–134. https://doi.org/10.1016/j.epsl.2005.02.008

Ferrand, T. P., Hilairet, N., Incel, S., Deldicque, D., Labrousse, L., Gasc, J., et al. (2017). Dehydration-driven stress transfer triggers intermediate-depth earthquakes. *Nature Communications*, *8*(1), 15247. https://doi.org/10.1038/ncomms15247

Fossen, H., & Cavalcante, G. C. G. (2017). Shear zones–A review. *Earth-Science Reviews*, *171*, 434–455. https://doi.org/10.1016/j.earscirev.2017.05.002

Frankel, S. P. (1950). Convergence rates of iterative treatments of partial differential equations. *Mathematics of Computation*, *4*(30), 65–75. https://doi.org/10.2307/2002770

Frohlich, C. (1989). The nature of deep-focus earthquakes. *Annual Review of Earth and Planetary Sciences*, *17*(1), 227–254. https://doi.org/10.1146/annurev.earth.17.1.227

Frohlich, C. (2006). *Deep earthquakes*. Cambridge University Press.

Fukao, Y., Widiyantoro, S., & Obayashi, M. (2001). Stagnant slabs in the upper and lower mantle transition region. *Reviews of Geophysics*, *39*(3), 291–323. https://doi.org/10.1029/1999rg000068

Fukuda, J. (2018). Variability of the space-time evolution of slow slip events off the Boso Peninsula, central Japan, from 1996 to 2014. *Journal of Geophysical Research: Solid Earth*, *123*(1), 732–760. https://doi.org/10.1002/2017jb014709

Gasc, J., Daigre, C., Moarefvand, A., Deldicque, D., Fauconnier, J., Gardonio, B., et al. (2022). Deep-focus earthquakes: From high-temperature experiments to cold slabs. *Geology*, *50*(9), 1018–1022. https://doi.org/10.1130/g50084.1

Gercek, H. (2007). Poisson's ratio values for rocks. *International Journal of Rock Mechanics and Mining Sciences*, *44*(1), 1–13. https://doi.org/10.1016/j.ijrmms.2006.04.011

Gerya, T. V. (2019). *Introduction to numerical geodynamic modelling*. Cambridge University Press.

Gerya, T. V., & Yuen, D. A. (2003). Characteristics-based marker-in-cell method with conservative finite-differences schemes for modeling geological flows with strongly variable transport properties. *Physics of the Earth and Planetary Interiors*, *140*(4), 293–318. https://doi.org/10.1016/j.pepi.2003.09.006

Goudarzi, M., Gerya, T., & Dinther, Y. v. (2023). A comparative analysis of continuum plasticity, viscoplasticity and phase-field models for earthquake sequence modeling. *Computational Mechanics*, *72*(4), 615–633. https://doi.org/10.1007/s00466-023-02311-0

Green, H. II., & Burnley, P. (1989). A new self-organizing mechanism for deep-focus earthquakes. *Nature*, *341*(6244), 733–737. https://doi.org/10.1038/341733a0

Griffith, W. A., Mitchell, T. M., Renner, J., & Di Toro, G. (2012). Coseismic damage and softening of fault rocks at seismogenic depths. *Earth and Planetary Science Letters*, *353*, 219–230. https://doi.org/10.1016/j.epsl.2012.08.013

Gruntfest, I. (1963). Thermal feedback in liquid flow; plane shear at constant stress. *Transactions of the Society of Rheology*, *7*(1), 195–207. https://doi.org/10.1122/1.548954

Hacker, B. R., Peacock, S. M., Abers, G. A., & Holloway, S. D. (2003). Subduction factory 2. Are intermediate-depth earthquakes in subducting slabs linked to metamorphic dehydration reactions? *Journal of Geophysical Research: Solid Earth*, *108*(B1). https://doi.org/10.1029/2001jb001129

Hacker, B. R., Yin, A., Christie, J. M., & Snoke, A. W. (1990). Differential stress, strain rate, and temperatures of mylonitization in the Ruby Mountains, Nevada: Implications for the rate and duration of uplift. *Journal of Geophysical Research: Solid Earth*, *95*(B6), 8569–8580. https://doi.org/10.1029/jb095ib06p08569

Hansen, L. N., Kumamoto, K. M., Thom, C. A., Wallis, D., Durham, W. B., Goldsby, D. L., et al. (2019). Low-temperature plasticity in olivine: Grain size, strain hardening, and the strength of the lithosphere. *Journal of Geophysical Research: Solid Earth*, *124*(6), 5427–5449. https://doi.org/10.1029/2018jb016736

Hayman, N. W., & Lavier, L. L. (2014). The geologic record of deep episodic tremor and slip. *Geology*, *42*(3), 195–198. https://doi.org/10.1130/g34990.1

Hirth, G., & Kohlstedt, D. L. (2003). Rheology of the upper mantle and the mantle wedge: A view from the experimentalists. *Geophysical Monograph-American Geophysical Union*, *138*, 83–106.

Hobbs, B., Mühlhaus, H.-B., & Ord, A. (1990). Instability, softening and localization of deformation. *Geological Society, London, Special Publications*, *54*(1), 143–165. https://doi.org/10.1144/gsl.sp.1990.054.01.15

Hobbs, B., Ord, A., & Teyssier, C. (1986). Earthquakes in the ductile regime? *Pure and Applied Geophysics*, *124*(1–2), 309–336. https://doi.org/10.1007/bf00875730

Houston, H. (2015). Deep earthquakes. In *Treatise on geophysics*. Elsevier.

Iordache, M.-M., & Willam, K. (1998). Localized failure analysis in elastoplastic Cosserat continua. *Computer Methods in Applied Mechanics and Engineering*, *151*(3–4), 559–586. https://doi.org/10.1016/s0045-7825(97)00166-7

Ito, E., & Sato, H. (1991). Aseismicity in the lower mantle by superplasticity of the descending slab. *Nature*, *351*(6322), 140–141. https://doi.org/10.1038/351140a0

Jacquey, A. B., Rattez, H., & Veveakis, M. (2021). Strain localization regularization and patterns formation in rate-dependent plastic materials with multiphysics coupling. *Journal of the Mechanics and Physics of Solids*, *152*, 104422. https://doi.org/10.1016/j.jmps.2021.104422

Jain, C., Korenaga, J., & Karato, S.-I. (2017). On the yield strength of oceanic lithosphere. *Geophysical Research Letters*, *44*(19), 9716–9722. https://doi.org/10.1002/2017gl075043

Jaquet, Y., Duretz, T., & Schmalholz, S. M. (2016). Dramatic effect of elasticity on thermal softening and strain localization during lithospheric shortening. *Geophysical Journal International*, *204*(2), 780–784. https://doi.org/10.1093/gji/ggv464

John, T., Medvedev, S., Rüpke, L. H., Andersen, T. B., Podladchikov, Y. Y., & Austrheim, H. (2009). Generation of intermediate-depth earthquakes by self-localizing thermal runaway. *Nature Geoscience*, *2*(2), 137–140. https://doi.org/10.1038/ngeo419

Karato, S.-I. (1984). Grain-size distribution and rheology of the upper mantle. *Tectonophysics*, *104*(1–2), 155–176. https://doi.org/10.1016/0040-1951(84)90108-2

Karato, S.-I. (2008). Preface. In *Deformation of earth materials: An introduction to the rheology of solid earth* (pp. ix–x). Cambridge University Press.

Kaus, B. J. P., de Montserrat, A., Medinger, N., Riel, N., Cosarinky, M., Berlie, N., et al. (2023). JuliaGeodynamics/GeoParams.jl: v0.5.1 [Software]. *Zenodo*. https://doi.org/10.5281/zenodo.10050339

Kaus, B. J. P., & Podladchikov, Y. Y. (2006). Initiation of localized shear zones in viscoelastoplastic rocks. *Journal of Geophysical Research: Solid Earth*, *111*(B4). https://doi.org/10.1029/2005jb003652

Kawazoe, T., Karato, S.-I., Otsuka, K., Jing, Z., & Mookherjee, M. (2009). Shear deformation of dry polycrystalline olivine under deep upper mantle conditions using a rotational Drickamer apparatus (RDA). *Physics of the Earth and Planetary Interiors*, *174*(1–4), 128–137. https://doi.org/10.1016/j.pepi.2008.06.027

Kelemen, P. B., & Hirth, G. (2007). A periodic shear-heating mechanism for intermediate-depth earthquakes in the mantle. *Nature*, *446*(7137), 787–790. https://doi.org/10.1038/nature05717

Kirby, S. H. (1987). Localized polymorphic phase transformations in high-pressure faults and applications to the physical mechanism of deep earthquakes. *Journal of Geophysical Research: Solid Earth*, *92*(B13), 13789–13800. https://doi.org/10.1029/jb092ib13p13789

Kirby, S. H., Stein, S., Okal, E. A., & Rubie, D. C. (1996). Metastable mantle phase transformations and deep earthquakes in subducting oceanic lithosphere. *Reviews of Geophysics*, *34*(2), 261–306. https://doi.org/10.1029/96rg01050

Kirkpatrick, J. D., Fagereng, Å., & Shelly, D. R. (2021). Geological constraints on the mechanisms of slow earthquakes. *Nature Reviews Earth & Environment*, *2*(4), 285–301. https://doi.org/10.1038/s43017-021-00148-w

Kiss, D., Podladchikov, Y. Y., Duretz, T., & Schmalholz, S. M. (2019). Spontaneous generation of ductile shear zones by thermal softening: Localization criterion, 1D to 3D modelling and application to the lithosphere. *Earth and Planetary Science Letters*, *519*, 284–296. https://doi.org/10.1016/j.epsl.2019.05.026

Kumamoto, K. M., Thom, C. A., Wallis, D., Hansen, L. N., Armstrong, D. E., Warren, J. M., et al. (2017). Size effects resolve discrepancies in 40 years of work on low-temperature plasticity in olivine. *Science Advances*, *3*(9), e1701338. https://doi.org/10.1126/sciadv.1701338

Li, M., Pranger, C., & van Dinther, Y. (2022). Characteristics of earthquake cycles: A cross-dimensional comparison of 0D to 3D numerical models. *Journal of Geophysical Research: Solid Earth*, *127*(8), e2021JB023726. https://doi.org/10.1029/2021jb023726

Lohman, R. B., & McGuire, J. J. (2007). Earthquake swarms driven by aseismic creep in the Salton Trough, California. *Journal of Geophysical Research: Solid Earth*, *112*(B4). https://doi.org/10.1029/2006jb004596

Mao, Z., Fan, D., Lin, J.-F., Yang, J., Tkachev, S. N., Zhuravlev, K., & Prakapenka, V. B. (2015). Elasticity of single-crystal olivine at high pressures and temperatures. *Earth and Planetary Science Letters*, *426*, 204–215. https://doi.org/10.1016/j.epsl.2015.06.045

McGuire, J. J., Wiens, D. A., Shore, P. J., & Bevis, M. G. (1997). The March 9, 1994 (M_w 7.6), deep Tonga earthquake: Rupture outside the seismically active slab. *Journal of Geophysical Research: Solid Earth*, *102*(B7), 15163–15182. https://doi.org/10.1029/96jb03185

Meade, C., & Jeanloz, R. (1991). Deep-focus earthquakes and recycling of water into the Earth's mantle. *Science*, *252*(5002), 68–72. https://doi.org/10.1126/science.252.5002.68

Miller, G. H., Stolper, E. M., & Ahrens, T. J. (1991). The equation of state of a molten komatiite: 2. Application to komatiite petrogenesis and the Hadean mantle. *Journal of Geophysical Research: Solid Earth*, *96*(B7), 11849–11864. https://doi.org/10.1029/91jb01203

Misra, S., & Mandal, N. (2007). Localization of plastic zones in rocks around rigid inclusions: Insights from experimental and theoretical models. *Journal of Geophysical Research: Solid Earth*, *112*(B9). https://doi.org/10.1029/2006jb004328

Moczo, P., Kristek, J., & Gális, M. (2014). *The finite-difference modelling of earthquake motions: Waves and ruptures*. Cambridge University Press.

Nishikawa, T., Ide, S., & Nishimura, T. (2023). A review on slow earthquakes in the Japan Trench. *Progress in Earth and Planetary Science*, *10*(1), 1–51. https://doi.org/10.1186/s40645-022-00528-w

Obara, K., & Kato, A. (2016). Connecting slow earthquakes to huge earthquakes. *Science*, *353*(6296), 253–257. https://doi.org/10.1126/science.aaf1512

Obata, M., & Karato, S.-I. (1995). Ultramafic pseudotachylite from the Balmuccia peridotite, Ivrea-Verbano zone, northern Italy. *Tectonophysics*, *242*(3–4), 313–328. https://doi.org/10.1016/0040-1951(94)00228-2

Ogawa, M. (1987). Shear instability in a viscoelastic material as the cause of deep focus earthquakes. *Journal of Geophysical Research: Solid Earth*, *92*(B13), 13801–13810. https://doi.org/10.1029/jb092ib13p13801

Okudaira, T., & Shigematsu, N. (2012). Estimates of stress and strain rate in mylonites based on the boundary between the fields of grain-size sensitive and insensitive creep. *Journal of Geophysical Research: Solid Earth*, *117*(B3). https://doi.org/10.1029/2011jb008799

Omlin, S., & Räss, L. (2024). High-performance xPU Stencil computations in Julia. *Proceedings of the JuliaCon Conferences*, *6*(64), 138. https://doi.org/10.21105/jcon.00138

Osako, M., Ito, E., & Yoneda, A. (2004). Simultaneous measurements of thermal conductivity and thermal diffusivity for garnet and olivine under high pressure. *Physics of the Earth and Planetary Interiors*, *143*, 311–320. https://doi.org/10.1016/j.pepi.2003.10.010

Paterson, M. S., & Wong, T.-F. (2005). *Experimental rock deformation: The brittle field* (Vol. 348). Springer.

Piccolo, A., Palin, R. M., Kaus, B. J. P., & White, R. W. (2019). Generation of Earth's early continents from a relatively cool Archean mantle. *Geochemistry, Geophysics, Geosystems*, *20*(4), 1679–1697. https://doi.org/10.1029/2018gc008079

Poirier, J. (1980). Shear localization and shear instability in materials in the ductile field. *Journal of Structural Geology*, *2*(1–2), 135–142. https://doi.org/10.1016/0191-8141(80)90043-7

Porkoláb, K., Moulas, E., & Schmalholz, S. M. (2025). Modeling the interplay between reaction progress, deformation and stress field evolution during antigorite dehydration: Implications for intermediate-depth seismicity. *Geophysical Research Letters*, *52*(10), e2024GL113865. https://doi.org/10.1029/2024gl113865

Prieto, G. A., Florez, M., Barrett, S. A., Beroza, G. C., Pedraza, P., Blanco, J. F., & Poveda, E. (2013). Seismic evidence for thermal runaway during intermediate-depth earthquake rupture. *Geophysical Research Letters*, *40*(23), 6064–6068. https://doi.org/10.1002/2013gl058109

Proietti, A., Bystricky, M., Guignard, J., Béjina, F., & Crichton, W. (2016). Effect of pressure on the strength of olivine at room temperature. *Physics of the Earth and Planetary Interiors*, *259*, 34–44. https://doi.org/10.1016/j.pepi.2016.08.004

Raleigh, C., & Paterson, M. (1965). Experimental deformation of serpentinite and its tectonic implications. *Journal of Geophysical Research*, *70*(16), 3965–3985. https://doi.org/10.1029/jz070i016p03965

Räss, L., Utkin, I., Duretz, T., Omlin, S., & Podladchikov, Y. Y. (2022). Assessing the robustness and scalability of the accelerated pseudo-transient method. *Geoscientific Model Development*, *15*(14), 5757–5786. https://doi.org/10.5194/gmd-15-5757-2022

Reber, J. E., Lavier, L. L., & Hayman, N. W. (2015). Experimental demonstration of a semi-brittle origin for crustal strain transients. *Nature Geoscience*, *8*(9), 712–715. https://doi.org/10.1038/ngeo2496

Reches, Z., & Lockner, D. A. (1994). Nucleation and growth of faults in brittle rocks. *Journal of Geophysical Research: Solid Earth*, *99*(B9), 18159–18173. https://doi.org/10.1029/94jb00115

Regenauer-Lieb, K., & Yuen, D. A. (2004). Positive feedback of interacting ductile faults from coupling of equation of state, rheology and thermal-mechanics. *Physics of the Earth and Planetary Interiors*, *142*(1–2), 113–135. https://doi.org/10.1016/j.pepi.2004.01.003

Riedel, M. R., & Karato, S.-I. (1997). Grain-size evolution in subducted oceanic lithosphere associated with the olivine-spinel transformation and its effects on rheology. *Earth and Planetary Science Letters*, *148*(1–2), 27–43. https://doi.org/10.1016/s0012-821x(97)00016-2

Rowe, C. D., Kirkpatrick, J. D., & Brodsky, E. E. (2012). Fault rock injections record paleo-earthquakes. *Earth and Planetary Science Letters*, *335*, 154–166. https://doi.org/10.1016/j.epsl.2012.04.015

Rubie, D. C., & Ross, C. R. II. (1994). Kinetics of the olivine-spinel transformation in subducting lithosphere: Experimental constraints and implications for deep slab processes. *Physics of the Earth and Planetary Interiors*, *86*(1–3), 223–243. https://doi.org/10.1016/0031-9201(94)05070-8

Rutter, E. (1986). On the nomenclature of mode of failure transitions in rocks. *Tectonophysics*, *122*(3–4), 381–387. https://doi.org/10.1016/0040-1951(86)90153-8

Schmalholz, S., & Duretz, T. (2015). Shear zone and nappe formation by thermal softening, related stress and temperature evolution, and application to the Alps. *Journal of Metamorphic Geology*, *33*(8), 887–908. https://doi.org/10.1111/jmg.12137

Schubnel, A., Brunet, F., Hilairet, N., Gasc, J., Wang, Y., & Green, H. W. (2013). Deep-focus earthquake analogs recorded at high pressure and temperature in the laboratory. *Science*, *341*(6152), 1377–1380. https://doi.org/10.1126/science.1240206

Schwartz, S. Y., & Rokosky, J. M. (2007). Slow slip events and seismic tremor at circum-Pacific subduction zones. *Reviews of Geophysics*, *45*(3). https://doi.org/10.1029/2006rg000208

Segall, P., & Bradley, A. M. (2012). Slow-slip evolves into megathrust earthquakes in 2D numerical simulations. *Geophysical Research Letters*, *39*(18). https://doi.org/10.1029/2012gl052811

Segall, P., Rubin, A. M., Bradley, A. M., & Rice, J. R. (2010). Dilatant strengthening as a mechanism for slow slip events. *Journal of Geophysical Research: Solid Earth*, *115*(B12). https://doi.org/10.1029/2010jb007449

Spang, A., Thielmann, M., & de Montserrat, A. (2025). Numerical model used in “Transient propagation of ductile ruptures by thermal runaway” [Software]. *Zenodo*. https://doi.org/10.5281/zenodo.14719483

Spang, A., Thielmann, M., & Kiss, D. (2024). Rapid ductile strain localization due to thermal runaway. *Journal of Geophysical Research: Solid Earth*, *129*(10), e2024JB028846. https://doi.org/10.1029/2024jb028846

Tao, W. C., & O'Connell, R. J. (1993). Deformation of a weak subducted slab and variation of seismicity with depth. *Nature*, *361*(6413), 626–628. https://doi.org/10.1038/361626a0

Tchalenko, J. (1970). Similarities between shear zones of different magnitudes. *Geological Society of America Bulletin*, *81*(6), 1625–1640. https://doi.org/10.1130/0016-7606(1970)81[1625:sbszod]2.0.co;2

The MathWorks Inc. (2022). Matlab version: 9.12.0 (r2022a) [Software]. *The MathWorks Inc*. https://www.mathworks.com

Thielmann, M. (2018). Grain size assisted thermal runaway as a nucleation mechanism for continental mantle earthquakes: Impact of complex rheologies. *Tectonophysics*, *746*, 611–623. https://doi.org/10.1016/j.tecto.2017.08.038

Thielmann, M., & Kaus, B. J. (2012). Shear heating induced lithospheric-scale localization: Does it result in subduction? *Earth and Planetary Science Letters*, *359*, 1–13. https://doi.org/10.1016/j.epsl.2012.10.002

Thielmann, M., Rozel, A., Kaus, B. J. P., & Ricard, Y. (2015). Intermediate-depth earthquake generation and shear zone formation caused by grain size reduction and shear heating. *Geology*, *43*(9), 791–794. https://doi.org/10.1130/g36864.1

Thomas, M. Y., Bhat, H. S., & Klinger, Y. (2017). Effect of brittle off-fault damage on earthquake rupture dynamics. *Fault zone dynamic processes: Evolution of fault properties during seismic rupture*, 255–280. https://doi.org/10.1002/9781119156895.ch14

Toffol, G., Yang, J., Pennacchioni, G., Faccenda, M., & Scambelluri, M. (2022). How to quake a subducting dry slab at intermediate depths: Inferences from numerical modelling. *Earth and Planetary Science Letters*, *578*, 117289. https://doi.org/10.1016/j.epsl.2021.117289

Turcotte, D. L., & Schubert, G. (2002). *Geodynamics*. Cambridge University Press.

Twiss, R., & Moores, E. (2007). *Structural geology*. Cambridge University Press

Uchida, N., Iinuma, T., Nadeau, R. M., Bürgmann, R., & Hino, R. (2016). Periodic slow slip triggers megathrust zone earthquakes in northeastern Japan. *Science*, *351*(6272), 488–492. https://doi.org/10.1126/science.aad3108

Vidale, J. E., & Shearer, P. M. (2006). A survey of 71 earthquake bursts across southern California: Exploring the role of pore fluid pressure fluctuations and aseismic slip as drivers. *Journal of Geophysical Research: Solid Earth*, *111*(B5). https://doi.org/10.1029/2005jb004034

Wada, I., Behn, M. D., & He, J. (2011). Grain-size distribution in the mantle wedge of subduction zones. *Journal of Geophysical Research: Solid Earth*, *116*(B10), B10203. https://doi.org/10.1029/2011jb008294

Wang, Y., Zhu, L., Shi, F., Schubnel, A., Hilairet, N., Yu, T., et al. (2017). A laboratory nanoseismological study on deep-focus earthquake micromechanics. *Science Advances*, *3*(7), e1601896. https://doi.org/10.1126/sciadv.1601896

Warren, J. M., & Hansen, L. N. (2023). Ductile deformation of the lithospheric mantle. *Annual Review of Earth and Planetary Sciences*, *51*(1), 581–609. https://doi.org/10.1146/annurev-earth-031621-063756

Weng, H., & Ampuero, J.-P. (2022). Integrated rupture mechanics for slow slip events and earthquakes. *Nature Communications*, *13*(1), 7327. https://doi.org/10.1038/s41467-022-34927-w

Yuen, D. A., Fleitout, L., Schubert, G., & Froidevaux, C. (1978). Shear deformation zones along major transform faults and subducting slabs. *Geophysical Journal International*, *54*(1), 93–119. https://doi.org/10.1111/j.1365-246x.1978.tb06758.x

Zhan, Z. (2020). Mechanisms and implications of deep earthquakes. *Annual Review of Earth and Planetary Sciences*, *48*(1), 147–174. https://doi.org/10.1146/annurev-earth-053018-060314

Zhang, L., Pellegrino, A., Townsend, D., & Petrinic, N. (2021). Temperature dependent dynamic strain localization and failure of ductile polymeric rods under large deformation. *International Journal of Mechanical Sciences*, *204*, 106563. https://doi.org/10.1016/j.ijmecsci.2021.106563

Zhang, Y., Yoshino, T., Yoneda, A., & Osako, M. (2019). Effect of iron content on thermal conductivity of olivine with implications for cooling history of rocky planets. *Earth and Planetary Science Letters*, *519*, 109–119. https://doi.org/10.1016/j.epsl.2019.04.048

References From the Supporting Information

Evans, B., & Goetze, C. (1979). The temperature variation of hardness of olivine and its implication for polycrystalline yield stress. *Journal of Geophysical Research: Solid Earth*, *84*(B10), 5505–5524. https://doi.org/10.1029/jb084ib10p05505

Gouriet, K., Cordier, P., Garel, F., Thoraval, C., Demouchy, S., Tommasi, A., & Carrez, P. (2019). Dislocation dynamics modelling of the power-law breakdown in olivine single crystals: Toward a unified creep law for the upper mantle. *Earth and Planetary Science Letters*, *506*, 282–291. https://doi.org/10.1016/j.epsl.2018.10.049

Kameyama, M., Yuen, D. A., & Karato, S.-I. (1999). Thermal-mechanical effects of low-temperature plasticity (the Peierls mechanism) on the deformation of a viscoelastic shear zone. *Earth and Planetary Science Letters*, *168*(1–2), 159–172. https://doi.org/10.1016/s0012-821x(99)00040-0

Long, H., Weidner, D. J., Li, L., Chen, J., & Wang, L. (2011). Deformation of olivine at subduction zone conditions determined from in situ measurements with synchrotron radiation. *Physics of the Earth and Planetary Interiors*, *186*(1–2), 23–35. https://doi.org/10.1016/j.pepi.2011.02.006

Mei, S., Suzuki, A., Kohlstedt, D., Dixon, N., & Durham, W. (2010). Experimental constraints on the strength of the lithospheric mantle. *Journal of Geophysical Research: Solid Earth*, *115*(B8). https://doi.org/10.1029/2009jb006873